On state and inertial parameter estimation of free-falling planar rigid bodies subject to unscheduled frictional impacts

Marco Gabiccini[a,1,*], Francesco Fusco[b,2]

[a] *Dipartimento di Ingegneria Civile e Industriale, Università di Pisa*
[b] *DANI Analitica s.r.l.*

Abstract

This paper addresses the problem of simultaneous state estimation and inertial and frictional parameter identification for planar rigid-bodies subject to *unscheduled* frictional impacts. The aim is to evaluate to what level of accuracy, given *noisy* captured poses of an object free-falling under gravity and impacting the surrounding environment, it is conceivable to reconstruct its states, the sequence of normal and tangential impulses and, concurrently, estimate its inertial properties along with Coulomb's coefficient of friction at contacts.

To this aim we set up a constrained nonlinear optimization problem, where the unscheduled impacts are handled via a complementarity formulation. To assess the validity of the proposed approach we test the identification results both (i) with respect to ground truth values produced with a simulator, and (ii) with respect to real experimental data. In both cases, we are able to provide accurate/realistic estimates of the inertia-to-mass ratio and friction coefficient along with a satisfactory reconstruction of systems states and contact impulses.

Keywords: Inertia estimation, contact dynamics, frictional impacts, nonlinear optimization.

1. Introduction and motivation

The possibility of identifying inertial parameters of objects undergoing passive trajectories in the presence of frictional contact can be beneficial to a wide range of fields. Therefore, it should not surprise that studies to solve this problem efficiently have been carried out for many years and for the most diverse applications. As an example, the ability to render a robot capable to autonomously learn the characteristics of an object, in order to dexterously manipulate it, to move it or simply to predict its trajectory, is a valuable resource which would greatly broaden the set of tasks that could be achieved with minimal human intervention.

One of the most intriguing scenarios that springs to mind, when dealing with inertia identification, is probably humanoid robotics. Here a robot needs to not only to estimate the inertia of objects it is going to interact with, but also to continuously track its own time-varying inertia, in order to balance properly while performing given tasks. Even in more classical scenarios like those typical of industrial manufacturing, the growing need for autonomy would greatly benefit from the implementation of handling systems which could autonomously decide upon the most appropriate way to manipulate objects undergoing various processes. For the above mentioned situations, and possibly many others, the knowledge of the inertial parameters involved is principal to develop controls without the need to rely on *a-priori* models, often incapable of accounting for the many variables governing complex tasks.

In this paper, we set out to investigate the possibility of identifying the inertial parameters of planar rigid objects undergoing frictional *unscheduled* impacts, with the sole knowledge of their motion as captured with

*Corresponding author. Phone: +39 050 221.80.77; Fax: +39 050 221 80 65.
Email addresses: marco.gabiccini@unipi.it (Marco Gabiccini), francesco.fusco1989@gmail.com (Francesco Fusco)
[1]Mail address: Largo L. Lazzarino 1, 56122 Pisa PI, Italy.
[2]Mail address: Viale Brianza 87, 20093 Cologno Monzese MI, Italy.

a low-cost vision system — with resolution and frame rate typical of a common action camera. While trying to achieve this goal, we introduce some novelties which fix some lacks and issues with other formulations. In particular: (i) we identify the friction coefficient between falling object and environment; (ii) instead of using raw data from the camera, along with its noise, we use those data to build a virtual trajectory, which fits the noisy one while remaining physically consistent. In this way, we have a noise filter built inside the identification formulation; (iii) we provide an identifiability analysis that explains the reason why using raw and noisy data is not a good idea in the context of inertia identification.

The envisioned application of our work is to endow a robot with the ability to learn the inertial properties of an object by watching its free-falling trajectories when it is thrown by another agent. In a developmental perspective, this would resamble how nonverbal babies learn the laws of physics and the properties of their toys, among other actions, by dropping them [1].

The paper is organized as follows: Sect. 2 provides motivations by analyzing a broad set of solutions proposed in the literature for inertial identification in different engineering disciplines and applications. The comparison is then focused towards scenarios closer to our contribution, namely inertial identification in the case of *free-falling objects undergoing unscheduled frictional impacts*.

In Sect. 3 we recall the time-stepping scheme behind the contact dynamics model used in our simulator, which makes use of a simple method to keep track of contact events. Even if state of the art methods are recalled, the main motivation for this section is to fix the notation for the rest of the paper. The formulation as a Nonlinear Programming Problem (NLP) of the whole framework and a procedure for its solution is provided as well.

In Sect. 4, after using the model adopted in Sect. 3 to generate simulated trajectories of a 2D object, we verify that the simulated motions give a realistic representation of contact events by analyzing impact values and the associated energy dissipation, thus proving that such formulation provides a physically consistent methodology for predicting the behaviour of a known object. Our results are also compared with those obtained with other formulations employed in the literature that make use of direct force-gap complementarity conditions, showing that only the approach we adopt gives realistic information that converge to asymptotic values as the time step decreases.

We then modify the presented formulation for identification purposes by proposing, in Sect. 5, a modified NLP that solves simultaneously the problem of state and parameter estimation. Here, an observability analysis is also performed to assess parameter identifiability under given conditions.

Section 6 shows the results of our identification method, applied to both simulated motions and real experiments. Conclusions and suggestions for future improvements are presented in Sect. 7.

2. Literature review

2.1. State and parameter estimation

In order to design efficient and robust controls for mechanical systems with contacts, one should be able to predict their behaviour with a sufficient level of realism. This requires accurate knowledge of the most relevant dynamic quantities such as body inertia, contact friction and restitution coefficient.

In a general estimation problem, one can propose a first classification of the contributions based on whether only the (time dependent) state of a system, only its (constant) parameters or both simultaneously should be estimated. A brief description of such problem categories can be found in [2], where also a variation of the widely used Extended Kalman Filter (EKF) for the resolution of nonlinear estimation problems is introduced.

Examples of *state estimation* can be found in [3], where the focus is on the estimation of pose and motion of objects in planar pushing tasks, in [4, 5], where vision and tactile information to estimate an object's state are combined, and in [6], where the use of contact sensors is made for the same purpose. In [7], Verscheure estimates contact parameters, namely stiffness and friction, thus solving a so-called *system estimation* problem. Among the contributions focused on *dual estimation*, i.e. the concurrent resolution of state and system estimation, we find [8] and [9], each devising a different version of the SLAM (Simultaneous

Localization And Mapping) problem, and [10], where the authors make use of a physics engine to render the estimation dynamically consistent.

According to the presented classification, our work belongs to the category of dual estimation. In fact, we combine state estimation and inertia and friction identification to fit a measured trajectory with a dynamic model where some parameters are unknown and should be estimated as well.

2.2. Inertia identification

If the focus of the estimation problem is towards object's inertia properties, namely mass, inertia tensor components and position of its center of mass, there are various reliable options, provided one can directly interact with the object under investigation by means of appropriate equipments. Surveys of methods for the identification of the above-mentioned inertia properties can be found in [11] or, for the particular case of modal analysis, in [12].

When the object is relatively accessible for the process, a modal analysis can be performed, as in [13] and [14], with the use of platforms on springs. A well rooted method for inertia identification requires the use of a multifilar pendulum. We find examples of such technique in [15], [16] or [17], where it is suggested to exploit a universal joint to cope with the issue of aligning the object's center of gravity with the axis of the pendulum. West [18] and Barreto [19] place the objects under investigation on Stewart platforms and measure the joint and the base forces and torques resulting from an imposed motion. A similar procedure is followed both in [20] and in [21], where the authors make use of appropriate measurement manipulators to impose the motion, as well as in [22], where a bench with rotating joints is devised, which is equipped with load cells.

The above methodologies can only be applied when the object under investigation is not in use for the duration of the measuring process, which often takes a long time. Our work, instead, tries to eliminate the need for physical interaction with the object, whose inertial properties should be identifiable while it is being operated by other agents.

2.3. Inertia self–identification

Examples of machines self-identification are common in literature. A reference case in the field is the one described by Atkeson in [23], who equipped a robotic manipulator with appropriate force and torque sensors to identify not only the inertia of a manipulated load, but also of its own links.

More recently, road vehicle inertia identification has become possible by means of on-board sensors as described in [24] and [25], with the possibility of exploiting also GPS information, as investigated in [26] and [27].

Although the above-mentioned works allow for identification of machines while they are in operation, the sensors' information required is very rich, diverse and still quite costly (forces, torques). While it may make sense for high-end vehicle applications, there are some fields which would greatly benefit from a reduction of the required sensors used in the identification process. That is why the formulation we present makes use of visual data only, as captured with a relatively low-cost camera, making it a fairly affordable solution for anyone.

2.4. Inertia identification from visual data

With the aim of reducing the needed data for identification, Ayusawa in [28] and [29] identifies a multibody system's inertia by measuring its posture with a motion capture equipment. The limits of his work, from our perspective, is that contact forces must be absent (as in the case of free-flying objects) or known through measurements. These assumptions, of course, eliminate the high nonlinearities connected with contact events which, instead, are the main challenge and contribution of our work.

With the precise aim of including contact events and contact forces in the inertia identification process, we find the work of Fazeli [30]. This paper is indeed the closest to ours, both in terms of goals and approach, and actually inspired our own research in this field. Our study is devised with the aim to improve upon results by Fazeli's paper by relaxing some of the hypotheses therein and resolving some of its issues. Similarly to [30] we setup a nonlinear problem (NLP) to reconstruct the trajectory of the identified object. However,

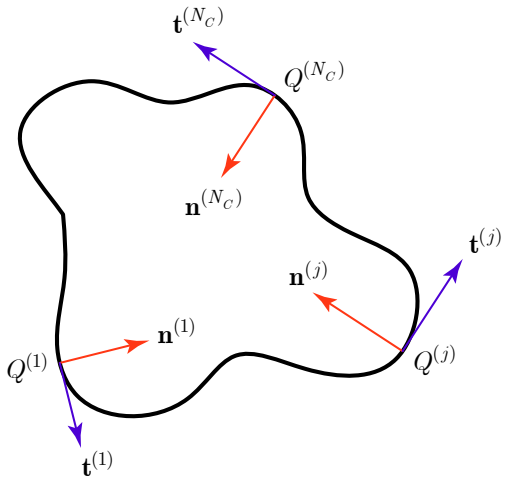

Figure 1: A representation of normal and tangential unit vectors forming the frames $\{S^{(j)}\} = \{Q^{(j)}; \boldsymbol{t}^{(j)}, \boldsymbol{n}^{(j)}\}$, for each contact point $Q^{(j)}$ of a generic 2D object.

in the process of performing inertia identification, we also present mainly the following improvements to state of the art methods: (i) provide an estimate for the unknown friction coefficient, and (ii) smoothen the reconstructed trajectory instead of making direct use of possibly very noisy data. Our contribution also extends to (iii) an original observability analysis to justify the need of reconstructing the object's trajectory instead of using the captured, noisy one.

A very interesting study where concurrent state and parameter estimation are performed in the context of contact and manipulation is [10]. However, here the estimation is focused mostly towards contact parameters, such as contact stiffness and friction, and the sensor data are much richer and costly than those provided by a single camera (ATI force and torques sensors, Vicon motion capture systems).

Similar studies on informative trajectories for identification, called *persistently exciting* (PE) trajectories can be found in [31] or [32]. However, these analyses make stricter assumptions on types of motions undergone by the system which are completely removed in our approach.

3. Simulation model – contact dynamics with restitution

In this section we present a dynamic simulation model with intermittent contacts that provides a sufficient level of realism in terms of contact impulses and energy dissipation to generate virtual experiments of an object free-falling and impacting the surrounding environment. This model is adapted from the time-stepping schemes originally proposed in [33] and [34]. Investigations on the efficiency of such schemes can be found in [35]. No original contributions are claimed in this section. Its motivation is mostly to establish the notation and present the relevant states and parameters of the system to be identified later. The simulated trajectories and the contact impulse sequences, generated with this model, will be used as ground truth values to be compare with the outcome of the identification program explained later in Sect. 5.

3.1. Dynamics

We consider a 2D environment and N_c contact forces acting on a single object at points $Q^{(j)}$, with $j = 1, \ldots, N_\mathrm{c}$. By attaching frame $\{S^{(j)}\} = \{Q^{(j)}; \boldsymbol{t}^{(j)}, \boldsymbol{n}^{(j)}\}$ to each contact point, where $\boldsymbol{n}^{(j)}$ and $\boldsymbol{t}^{(j)}$ are, respectively, the inward normal and tangent unit vectors to the object's boundary, the corresponding contact force $\boldsymbol{f}_\mathrm{c}^{(j)}$ can be decomposed in its normal and tangential components as $\boldsymbol{f}_\mathrm{c}^{(j)} = f_\mathrm{n}^{(j)} \boldsymbol{n}^{(j)} + f_\mathrm{t}^{(j)} \boldsymbol{t}^{(j)}$, as in Figure 1.

By labelling forces as conservative, contact-generated, and external ones, respectively, the *Newton-Euler* equations of motion of the object can be written as follows

$$\mathbf{M}\dot{\boldsymbol{v}} + \mathbf{K}(\boldsymbol{q}, \boldsymbol{v}) = -\nabla\mathbf{V} + \mathbf{G}\boldsymbol{\sigma} + \boldsymbol{f}_{\text{ext}} \tag{1}$$

$$\boldsymbol{v} = \dot{\boldsymbol{q}} \tag{2}$$

where:

- $\boldsymbol{q} = (x \quad y \quad \theta)^T \in \mathbb{R}^3$ is object's configuration, with x and y coordinates of its center of mass (COM) and θ its orientation with respect to a fixed frame;
- $\boldsymbol{v} = (v_x \quad v_y \quad \omega)^T \in \mathbb{R}^3$ is the object's velocity, with v_x, v_y linear velocities of its COM and ω its angular velocity with respect to a fixed frame;
- $\mathbf{M} := \texttt{diag}\,(m,\, m,\, J) \in \mathbb{R}^{3\times 3}$ is the object's inertia matrix, m being its mass and J its moment of inertia with respect to the COM;
- $\mathbf{K} = \mathbf{K}(\boldsymbol{q}, \boldsymbol{v}) \in \mathbb{R}^3$ is the vector containing the object's gyroscopic terms;
- $\nabla\mathbf{V} = \nabla\mathbf{V}(\boldsymbol{q}) \in \mathbb{R}^3$ is the gradient of the potential energy, which gives the resultant of the conservative forces;
- $\mathbf{G} = \mathbf{G}(\boldsymbol{q}) = (\mathbf{N}(\boldsymbol{q}) \quad \mathbf{T}(\boldsymbol{q})) \in \mathbb{R}^{3\times 2N_{\text{c}}}$ is the generalized *grasp* matrix, built with matrices $\mathbf{N}(\boldsymbol{q}) \in \mathbb{R}^{3\times N_{\text{c}}}$ and $\mathbf{T}(\boldsymbol{q}) \in \mathbb{R}^{3\times N_{\text{c}}}$ which map, respectively, normal and tangential contact forces at each $Q^{(j)}$ into wrenches with respect to the COM and appear explicitly as follows

$$\begin{array}{rcl} \mathbf{N}(\boldsymbol{q}) & = & \left(\begin{array}{ccc} \mathbf{N}(\boldsymbol{q})^{(1)} & \cdots & \mathbf{N}(\boldsymbol{q})^{(N_{\text{c}})} \end{array}\right), \\ \mathbf{T}(\boldsymbol{q}) & = & \left(\begin{array}{ccc} \mathbf{T}(\boldsymbol{q})^{(1)} & \cdots & \mathbf{T}(\boldsymbol{q})^{(N_{\text{c}})} \end{array}\right); \end{array} \tag{3}$$

- $\boldsymbol{\sigma} = \left(\boldsymbol{\sigma}_{\text{n}}^T \quad \boldsymbol{\sigma}_{\text{t}}^T\right)^T \in \mathbb{R}^{2N_{\text{c}}}$ is the vector where all the normal and tangential components of the contact forces are stacked:

$$\boldsymbol{\sigma}_{\text{n}} = \left(\begin{array}{ccc} f_{\text{n}}^{(1)} & \cdots & f_{\text{n}}^{(N_{\text{c}})} \end{array}\right)^T, \qquad \boldsymbol{\sigma}_{\text{t}} = \left(\begin{array}{ccc} f_{\text{t}}^{(1)} & \cdots & f_{\text{t}}^{(N_{\text{c}})} \end{array}\right)^T;$$

- $\boldsymbol{f}_{\text{ext}} \in \mathbb{R}^3$ is the resultant of external non-conservative forces acting on the body, if any.

3.2. Restitution

To determine whether an object makes contact with the environment and which components of force are involved, we first look at the state of the gap, following the considerations formulated in [36] for a single point contact.

For the j-th contact pair, the *normal gap* $g_{\text{n}}^{(j)}(\boldsymbol{q})$ is the distance between points on the object and the environment that are "most likely" to make contact; in the case of object and environment locally convex around $Q^{(j)}$, $g_{\text{n}}^{(j)}(\boldsymbol{q})$ is the minimum distance between the two. The normal gap is a scalar quantity that is positive (> 0) when there is no contact, negative (< 0) when there is interpenetration and equal to zero ($= 0$) if there is contact.

The time derivative of $g_{\text{n}}^{(j)}(\boldsymbol{q})$, here denoted as *separation velocity* $\dot{g}_{\text{n}}^{(j)}(\boldsymbol{q}, \boldsymbol{v})$, represents the rate at which the gap opens. If it is negative, the object is moving towards the environment, reducing the gap and possibly making contact.

By using the above-mentioned quantities, it is possible to make a distinction among four possible situations, as shown in Figure 2. No contact force is present when either the body is separated (case 1: $g_{\text{n}}^{(j)}(\boldsymbol{q}) > 0$) or moving away from the environment (case 4: $\dot{g}_{\text{n}}^{(j)}(\boldsymbol{q}, \boldsymbol{v}) > 0$). The conditions in which contact forces are present are those of *impulsive* contact. These happen when the two bodies are either moving towards each

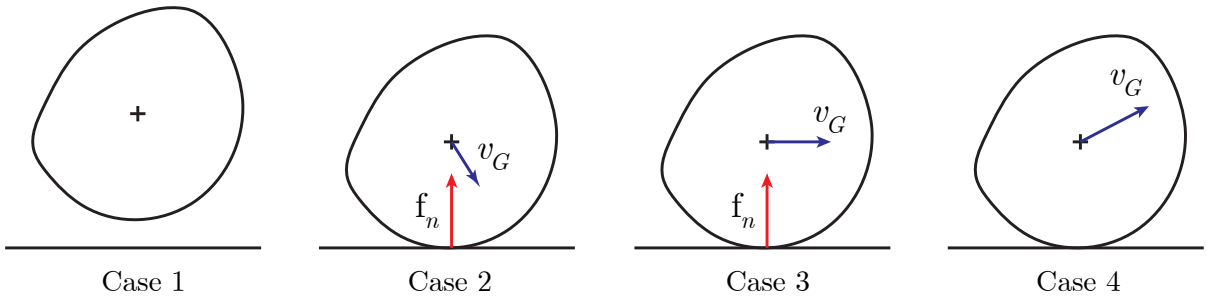

Figure 2: Four possible contact states. Case 1: $g_{\mathrm{n}}^{(j)}(\boldsymbol{q}) > 0$ (no impulse); Case 2: $g_{\mathrm{n}}^{(j)}(\boldsymbol{q}) = 0$ and $\dot{g}_{\mathrm{n}}^{(j)}(\boldsymbol{q}, \boldsymbol{v}) < 0$ (impulse); Case 3: $g_{\mathrm{n}}^{(j)}(\boldsymbol{q}) = 0$ and $\dot{g}_{\mathrm{n}}^{(j)}(\boldsymbol{q}, \boldsymbol{v}) = 0$ (impulse); Case 4: $g_{\mathrm{n}}^{(j)}(\boldsymbol{q}) = 0$ and $\dot{g}_{\mathrm{n}}^{(j)}(\boldsymbol{q}, \boldsymbol{v}) > 0$. (no impulse).

other from a tangent condition (case 2: $g_{\mathrm{n}}^{(j)}(\boldsymbol{q}) = 0$, $\dot{g}_{\mathrm{n}}^{(j)}(\boldsymbol{q}, \boldsymbol{v}) < 0$), or in the event of *prolonged* contact (case 3: $g_{\mathrm{n}}^{(j)}(\boldsymbol{q}) = 0$, $\dot{g}_{\mathrm{n}}^{(j)}(\boldsymbol{q}, \boldsymbol{v}) = 0$), when the velocity field keeps the body in tangent contact with the environment.

To include all the above possible states in our formulation we use the classical *Newtonian approach* to contact [37]. The restitution coefficient ε, with $0 \leq \varepsilon \leq 1$, is introduced to model contact elasticity; its value ranges from completely inelastic ($\varepsilon = 0$) to perfectly elastic ($\varepsilon = 1$) contact.

The relation between normal contact force $f_{\mathrm{n}}^{(j)}$ and kinematic state of contact is then given by the *restitution* conditions

$$\begin{aligned} f_{\mathrm{n}}^{(j)} &\geq 0 \\ \dot{g}_{\mathrm{n}}^{(j)}(\boldsymbol{q}, \boldsymbol{v}^+) + \varepsilon\, \dot{g}_{\mathrm{n}}^{(j)}(\boldsymbol{q}, \boldsymbol{v}) &\geq 0 \\ f_{\mathrm{n}}^{(j)} \left(\dot{g}_{\mathrm{n}}^{(j)}(\boldsymbol{q}, \boldsymbol{v}^+) + \varepsilon\, \dot{g}_{\mathrm{n}}^{(j)}(\boldsymbol{q}, \boldsymbol{v}) \right) &= 0 \end{aligned} \tag{4}$$

where $\boldsymbol{v}^+$ is object's velocity immediately after contact has occurred.

Conditions in Eq. (4), abbreviated as $0 \leq f_{\mathrm{n}}^{(j)} \perp \left(\dot{g}_{\mathrm{n}}^{(j)}(\boldsymbol{q}, \boldsymbol{v}^+) + \varepsilon\, \dot{g}_{\mathrm{n}}^{(j)}(\boldsymbol{q}, \boldsymbol{v}) \right) \geq 0$, are the well known *complementarity conditions* [38]. These are introduced to cope with mutually exclusive conditions and are highly nonlinear.

In our case, by activating Eqs. (4) *if and only if* the gap is closed ($g_{\mathrm{n}}^{(j)}(\boldsymbol{q}) = 0$), we ensure that the change in contact normal velocity $\dot{g}_{\mathrm{n}}^{(j)}(\boldsymbol{q}, \boldsymbol{v})$ is associated with (and caused by) a contact force $f_{\mathrm{n}}^{(j)}$ acting on the object as a result of a collision, as shown in Figure 3.

There exists a number of proposed corrections that render complementarity problems more easily solvable, but the drawback is often to smoothen them. This is certainly an issue when modelling rigid-body contacts, because contact forces are often impulsive; smoothed complementarity condition would tend to distribute the contact impulse in a time window that is too wide for a rigid-body contact, thus reducing physical plausibility.

We propose, instead, a solution that turns the contact phenomenon into an *on/off* condition. To this aim, we transform restitution conditions in Eqs. (4) into *Mixed Integer* conditions. *Mixed Integer Programming* is used when some variables are required to assume only integer values; in our case, by following the so called *Big-M* method [39], we introduce a scalar quantity H, sufficiently large for our purposes, and two variables for each j-th contact, $z_{\mathrm{c}}^{(j)}$ and $z_{\mathrm{nc}}^{(j)}$, whose values are either 0 or 1. We then write the conditions as

$$\begin{gathered} 0 \leq f_{\mathrm{n}}^{(j)} \leq H z_{\mathrm{c}}^{(j)} \\ -H z_{\mathrm{nc}}^{(j)} \leq \dot{g}_{\mathrm{n}}^{(j)}(\boldsymbol{q}, \boldsymbol{v}^+) + \varepsilon\, \dot{g}_{\mathrm{n}}^{(j)}(\boldsymbol{q}, \boldsymbol{v}) \leq H z_{\mathrm{nc}}^{(j)} \\ z_{\mathrm{c}}^{(j)} + z_{\mathrm{nc}}^{(j)} \leq 1, \end{gathered} \tag{5}$$

where variables $z_{\mathrm{c}}^{(j)}$ and $z_{\mathrm{nc}}^{(j)}$ are not part of the problem's solution, but are introduced to keep track of active contacts. This means that the third equation from Eqs. (5) will not be part of our formulation; the values of $z_{\mathrm{c}}^{(j)}$ and $z_{\mathrm{nc}}^{(j)}$ are, instead, imposed by monitoring $g_{\mathrm{n}}^{(j)}(\boldsymbol{q})$ and $\dot{g}_{\mathrm{n}}^{(j)}(\boldsymbol{q},\boldsymbol{v})$ and setting

$$\begin{pmatrix} z_{\mathrm{c}}^{(j)} \\ z_{\mathrm{nc}}^{(j)} \end{pmatrix} = \begin{cases} \begin{pmatrix} 0 \\ 1 \end{pmatrix} \text{ if } g_{\mathrm{n}}^{(j)}(\boldsymbol{q}) > 0 \bigvee \dot{g}_{\mathrm{n}}^{(j)}(\boldsymbol{q},\boldsymbol{v}) > 0 \\ \\ \begin{pmatrix} 1 \\ 0 \end{pmatrix} \text{ if } g_{\mathrm{n}}^{(j)}(\boldsymbol{q}) \leq 0 \bigwedge \dot{g}_{\mathrm{n}}^{(j)}(\boldsymbol{q},\boldsymbol{v}) \leq 0 \end{cases} \tag{6}$$

In this manner the appropriate constraint from Eqs. (5) is toggled.

Restitution conditions are incompatible with conditions that impose gap closure when contact force is present, i.e. $0 \leq f_{\mathrm{n}}^{(j)} \perp g_{\mathrm{n}}^{(j)}(\boldsymbol{q}) \geq 0$; the first conditions are, in fact, the differentiated form of the latter [37]. We therefore tolerate a small interpenetration between body and environment ($g_{\mathrm{n}}(\boldsymbol{q}) < 0$). However, interpenetration can be reduced by using a smaller time step h in the time discretization, as it will be shown in Sect. 3.5.

To write Eqs. (5) for all N_{c} contacts on the body, we can exploit the fact that matrix $\mathbf{N}(\boldsymbol{q})$, which maps normal contact forces into their contribution to the wrench at the COM, can be transposed to obtain a map from object's velocity $\boldsymbol{v}$ to the separation velocities $\dot{g}_{\mathrm{n}}^{(j)}$ for all contacts. In so doing, we obtain

$$\begin{aligned} 0 \leq \boldsymbol{\sigma}_{\mathrm{n}} \leq H\boldsymbol{z}_{\mathrm{c}} \\ -H\boldsymbol{z}_{\mathrm{nc}} \leq \mathbf{N}(\boldsymbol{q})^T(\boldsymbol{v}^+ + \varepsilon\,\boldsymbol{v}) \leq H\boldsymbol{z}_{\mathrm{nc}}, \end{aligned} \tag{7}$$

where $\boldsymbol{z}_{\mathrm{c}} = \begin{pmatrix} z_{\mathrm{c}}^{(1)} & \cdots & z_{\mathrm{c}}^{(N_{\mathrm{c}})} \end{pmatrix} \in \mathbb{R}^{N_{\mathrm{c}}}$ and $\boldsymbol{z}_{\mathrm{nc}} = \begin{pmatrix} z_{\mathrm{nc}}^{(1)} & \cdots & z_{\mathrm{nc}}^{(N_{\mathrm{c}})} \end{pmatrix} \in \mathbb{R}^{N_{\mathrm{c}}}$. Their components are, again, imposed as in Eq. (6).

3.3. Friction

Frictional forces are regulated by the *Maximum Dissipation Principle* [40]. This principle states that the feasible set of tangential contact forces $f_{\mathrm{t}}^{(j)}$ is the one that maximizes the rate of energy dissipation. Using the *tangential basis* $\mathbf{T}(\boldsymbol{q})$ to consider the effects of all frictional forces on the COM, the power *dissipated* by

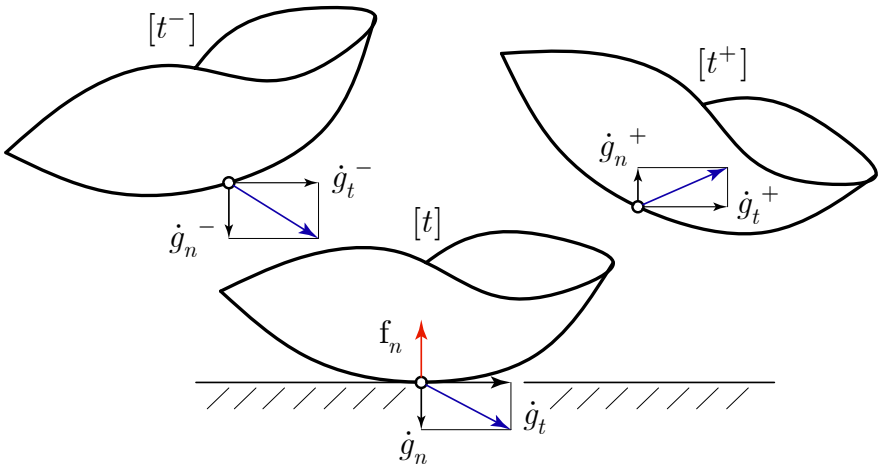

Figure 3: Effect of Eqs. (4), activated for a posture $\boldsymbol{q}$ associated with $g_{\mathrm{n}}^{(j)}(\boldsymbol{q}) = 0$. A contact point approaching the environment with normal velocity $\dot{g}_{\mathrm{n}}^{(j)}(\boldsymbol{q},\boldsymbol{v})$ is subject to an inversion of its motion caused by a contact force $f_{\mathrm{n}}^{(j)}$. After the impact, its normal velocity becomes $\dot{g}_{\mathrm{n}}^{(j)}(\boldsymbol{q},\boldsymbol{v}^+) = -\varepsilon\dot{g}_{\mathrm{n}}^{(j)}(\boldsymbol{q},\boldsymbol{v})$.

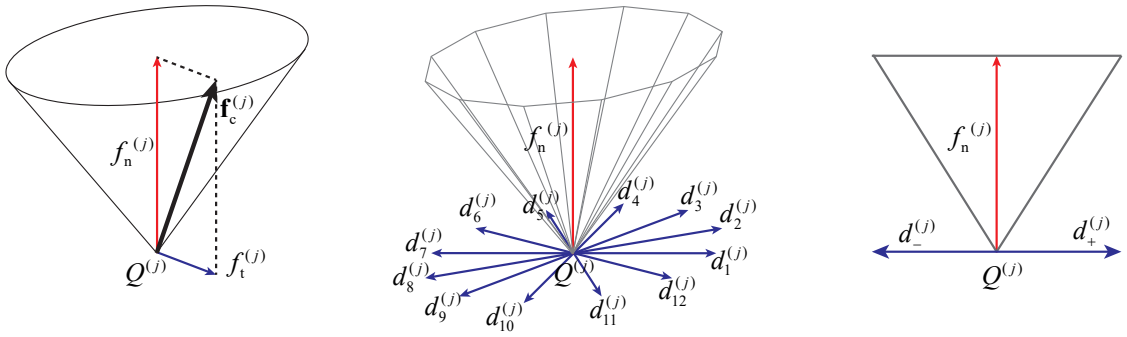

(a) Friction cone in 3D (b) Friction pyramid in 3D (c) Friction pyramid in 2D

Figure 4: Approximation of the 3D friction cone (Figure 4(a)) as a 3D pyramid (Figure 4(b)) with positive spanning unit vectors $\vec{d}_l$, with $l = 1, \ldots, p$. In Figure 4(c), exact description of the friction cone in 2D by the two positive spanning unit vectors $\vec{d}_+$ and $\vec{d}_-$.

friction on the body can be written as $W_{\text{diss}} = -\boldsymbol{v}^T \mathbf{T}(\boldsymbol{q})\boldsymbol{\sigma}_t$. Since the objective is to maximize dissipation, we search for the tangential forces that solve the minimum problem

$$\begin{aligned} \min_{\boldsymbol{\sigma}_t} \quad & \boldsymbol{v}^T \mathbf{T}(\boldsymbol{q})\boldsymbol{\sigma}_t \\ \text{s.t.} \quad & \Phi(f_t^{(j)}) \leq \mu f_n^{(j)} \qquad \forall j \end{aligned} \tag{8}$$

where $\Phi(f_t^{(j)})$ is a friction law that describes the set of feasible tangential forces and μ is the coefficient of friction.

In order to solve the *Constrained Optimization Problem* (8), we introduce a vector of *Lagrangian multipliers* $\boldsymbol{\lambda} = (\lambda^{(1)} \cdots \lambda^{(N_c)})^T \in \mathbb{R}^{N_c}$, and the *Lagrangian*:

$$L(\boldsymbol{\sigma}_t, \boldsymbol{\lambda}) = \boldsymbol{v}^T \mathbf{T}(\boldsymbol{q})\boldsymbol{\sigma}_t + \sum_{j=1}^{N_c} \lambda^{(j)} \left(\Phi(f_t^{(j)}) - \mu f_n^{(j)} \right)$$

The solution must then satisfy the *Karush-Kuhn-Tucker conditions* (KKT) [41]:

$$\begin{aligned} \frac{\partial L(\boldsymbol{\sigma}_t, \boldsymbol{\lambda})}{\partial \boldsymbol{\sigma}_t} = \mathbf{T}(\boldsymbol{q})^T \boldsymbol{v} + \sum_{j=1}^{N_c} \lambda^{(j)} \frac{\partial \Phi(f_t^{(j)})}{\partial \boldsymbol{\sigma}_t} &= 0 \\ \boldsymbol{\lambda} &\geq 0 \\ \mu f_n^{(j)} - \Phi(f_t^{(j)}) &\geq 0, \forall j \\ \lambda^{(j)} \left(\mu f_n^{(j)} - \Phi(f_t^{(j)}) \right) &= 0, \forall j \end{aligned} \tag{9}$$

3.4. Friction law and its discretization

The set of feasible frictional forces will be given by the *Coulomb's friction law* which, considering the general case of 3D contact and the tangential force vector $\boldsymbol{f}_t^{(j)} \in \mathbb{R}^3$, takes the form $\Phi(\boldsymbol{f}_t^{(j)}) = \|\boldsymbol{f}_t^{(j)}\|_2$. By substituting the above law in Eqs. (8) and (9), we bound the j-th contact force $\boldsymbol{f}_c^{(j)} = \boldsymbol{f}_t^{(j)} + f_n^{(j)} \boldsymbol{n}^{(j)}$ to lie inside the *friction cone* as shown in Figure 4, and to be described by $\|\boldsymbol{f}_t^{(j)}\|_2 \leq \mu f_n^{(j)}$.

Since the friction cone introduces a strong non-linearity [37], an approximated form is usually employed instead. The tangent plane for each contact will be spanned by p unit vectors $\vec{d}_l^{(j)} \in \mathbb{R}^3$, with $l = 1, \ldots, p$, originating from the contact point $Q^{(j)}$, so that the cone is substituted with a *pyramid*, as in Figure 4.

Contact force $\boldsymbol{f}_{\mathrm{c}}^{(j)}$ is then defined as the positive vector sum

$$\boldsymbol{f}_{\mathrm{c}}^{(j)} = f_{\mathrm{n}}^{(j)} \boldsymbol{n}^{(j)} + \sum_{l=1}^{p} f_{\mathrm{t},l}^{(j)} \, \vec{d}_l^{(j)}, \qquad f_{\mathrm{t},l}^{(j)} \geq 0,$$

and the friction law becomes $\Phi(\boldsymbol{f}_{\mathrm{t}}^{(j)}) = \sum_{l=1}^{p} f_{\mathrm{t},l}^{(j)}$. We build a tangential basis $\mathbf{T}_l(\boldsymbol{q})^{(j)}$ for each direction vector $\vec{d}_l^{(j)}$ relative to the j-th contact, and then juxtapose the contributions from all the p directions. By so doing, we obtain $\widetilde{\mathbf{T}}(\boldsymbol{q})^{(j)} = (\mathbf{T}_1(\boldsymbol{q})^{(j)} \quad \cdots \quad \mathbf{T}_p(\boldsymbol{q})^{(j)})$, which is the discretized equivalent of basis $\mathbf{T}(\boldsymbol{q})^{(j)}$ for the tangential forces acting on each contact point $Q^{(j)}$. The global tangential basis $\widetilde{\mathbf{T}}(\boldsymbol{q})$, which incorporates the contributions from all the N_{c} contacts on the body, is then obtained as:

$$\widetilde{\mathbf{T}}(\boldsymbol{q}) = (\widetilde{\mathbf{T}}(\boldsymbol{q})^{(1)} \quad \cdots \quad \widetilde{\mathbf{T}}(\boldsymbol{q})^{(N_{\mathrm{c}})})$$

which has the same form of $\mathbf{T}(\boldsymbol{q})$ in Eq. (3).

For a 2D contact, the friction pyramid is an *exact* description of the friction cone which is reduced to a triangle with two opposite direction vectors $\vec{d}_l^{(j)}$ $(l = 1, 2)$, as in Figure 4. We name these vectors $\vec{d}_+^{(j)}$ and $\vec{d}_-^{(j)}$ and the associated tangential forces $f_{\mathrm{t},+}^{(j)}$ and $f_{\mathrm{t},-}^{(j)}$. The dimensions of the newly obtained matrices are, in this case, $\mathbf{T}_l(\boldsymbol{q})^{(j)} \in \mathbb{R}^{3\times 1}$, $\widetilde{\mathbf{T}}(\boldsymbol{q})^{(j)} \in \mathbb{R}^{3\times 2}$ and $\widetilde{\mathbf{T}}(\boldsymbol{q}) \in \mathbb{R}^{3\times 2N_{\mathrm{c}}}$.

By writing the KKT conditions in Eq. (9) for all N_{c} contacts on the body, and employing the newly obtained friction pyramid for 2D contacts, we obtain the set of equations that will model friction in our formulation

$$\begin{aligned}
\boldsymbol{\lambda} &\geq 0 && (10)\\
\widetilde{\boldsymbol{\sigma}}_{\mathrm{t}} &\geq 0 && (11)\\
\mu\, \boldsymbol{\sigma}_{\mathrm{n}} - \mathbf{E}^T \widetilde{\boldsymbol{\sigma}}_{\mathrm{t}} &\geq 0 && (12)\\
\boldsymbol{\lambda}^T \left(\mu\, \boldsymbol{\sigma}_{\mathrm{n}} - \mathbf{E}^T \widetilde{\boldsymbol{\sigma}}_{\mathrm{t}}\right) &= 0 && (13)\\
\widetilde{\mathbf{T}}(\boldsymbol{q})^T \boldsymbol{v} + \mathbf{E}\, \boldsymbol{\lambda} &\geq 0 && (14)\\
\widetilde{\boldsymbol{\sigma}}_{\mathrm{t}}^T \left(\widetilde{\mathbf{T}}(\boldsymbol{q})^T \boldsymbol{v} + \mathbf{E}\, \boldsymbol{\lambda}\right) &= 0 && (15)
\end{aligned}$$

where $\widetilde{\boldsymbol{\sigma}}_{\mathrm{t}} = (\ f_{\mathrm{t},+}^{(1)} \quad f_{\mathrm{t},-}^{(1)} \quad \cdots \quad f_{\mathrm{t},+}^{(N_{\mathrm{c}})} \quad f_{\mathrm{t},-}^{(N_{\mathrm{c}})}\ )^T \in \mathbb{R}^{2N_{\mathrm{c}}}$ is the vector where all the components of the tangential forces are stacked, $\mathbf{E} := \mathtt{diag}(\boldsymbol{e}, \ldots, \boldsymbol{e}) \in \mathbb{R}^{pN_{\mathrm{c}}\times N_{\mathrm{c}}}$ is a diagonal block matrix with $\boldsymbol{e} = (1 \cdots 1)^T \in \mathbb{R}^p$, and Eq. (15) is the direct consequence of prescribing non-negativity for all the terms in $\widetilde{\boldsymbol{\sigma}}_{\mathrm{t}}$ (Eq. (11)).

Conditions in Eqs. (10)–(15) can be written more compactly in the form of complementarity conditions as $0 \leq \boldsymbol{\lambda} \perp \left(\mu\, \boldsymbol{\sigma}_{\mathrm{n}} - \mathbf{E}^T \widetilde{\boldsymbol{\sigma}}_{\mathrm{t}}\right) \geq 0$ and $0 \leq \widetilde{\boldsymbol{\sigma}}_{\mathrm{t}} \perp \left(\widetilde{\mathbf{T}}(\boldsymbol{q})^T \boldsymbol{v} + \mathbf{E}\, \boldsymbol{\lambda}\right) \geq 0$.

3.5. Time-stepping scheme

To setup a simulation model for an object in dynamic contact with a 2D environment, we collect Eqs. (1), (7) and (10)–(15) and apply a discretization scheme based on the *Implicit Euler* method [33]. Therefore, we approximate derivatives as $\boldsymbol{v} = \mathrm{d}\boldsymbol{q}/\mathrm{d}t \Rightarrow \boldsymbol{v}^{k+1} = (\boldsymbol{q}^{k+1} - \boldsymbol{q}^k)/h$, where superscripts k and $k+1$ denote two subsequent time instants and h is the time interval $h = t^{k+1} - t^k$. This formulation requires the use of force integrals instead of instantaneous forces, which we obtain as $\boldsymbol{c}_{\mathrm{n}} = \int_{t^k}^{t^{k+1}} \boldsymbol{\sigma}_{\mathrm{n}}\, \mathrm{d}t$ and $\boldsymbol{c}_{\mathrm{t}} = \int_{t^k}^{t^{k+1}} \widetilde{\boldsymbol{\sigma}}_{\mathrm{t}}\, \mathrm{d}t$.

The time-stepping scheme resulting from the discretization is then given by the *dynamic* and *kinematic reconstruction* equations

$$\mathbf{M}(\boldsymbol{v}^{k+1} - \boldsymbol{v}^k) + h\mathbf{K}(\boldsymbol{q}^k, \boldsymbol{v}^k)\boldsymbol{v}^k = \widetilde{\mathbf{G}}(\boldsymbol{q}^k)\boldsymbol{c}^{k+1} + h\left[\boldsymbol{f}_{\mathrm{ext}}^k - \nabla \mathbf{V}(\boldsymbol{q}^k)\right], \tag{16}$$

$$h\, \boldsymbol{v}^{k+1} - \boldsymbol{q}^{k+1} + \boldsymbol{q}^k = 0, \tag{17}$$

by the *complementarity* and *inequality* equations

$$\begin{aligned} 0 \leq \boldsymbol{\lambda}^{k+1} \perp \ & \left(\mu\, \boldsymbol{c}_{\mathrm{n}}^{k+1} - \mathbf{E}^T \boldsymbol{c}_{\mathrm{t}}^{k+1}\right) \geq 0, \\ 0 \leq \boldsymbol{c}_{\mathrm{t}}^{k+1} \perp \ & \left(\widetilde{\mathbf{T}}(\boldsymbol{q}^k)^T \boldsymbol{v}^{k+1} + \mathbf{E}\, \boldsymbol{\lambda}^{k+1}\right) \geq 0, \end{aligned} \tag{18}$$

and by the *additional inequality* equations

$$\begin{aligned} \boldsymbol{c}_{\mathrm{n}}^{k+1} \geq & 0, \\ H \boldsymbol{z}_{\mathrm{c}}^{k+1} - \boldsymbol{c}_{\mathrm{n}}^{k+1} \geq & 0, \\ \mathbf{N}(\boldsymbol{q})^T \left(\boldsymbol{v}^{k+1} + \varepsilon\, \boldsymbol{v}^k\right) \geq & - H \boldsymbol{z}_{\mathrm{nc}}^{k+1}, \\ \mathbf{N}(\boldsymbol{q})^T \left(\boldsymbol{v}^{k+1} + \varepsilon\, \boldsymbol{v}^k\right) \leq & + H \boldsymbol{z}_{\mathrm{nc}}^{k+1}. \end{aligned} \tag{19}$$

Here, $\widetilde{\mathbf{G}}(\boldsymbol{q}^k) = (\mathbf{N}(\boldsymbol{q}^k) \quad \widetilde{\mathbf{T}}(\boldsymbol{q}^k)) \in \mathbb{R}^{3\times(1+pN_{\mathrm{c}})}$ is the generalized grasp matrix for the discretized case.

The active contacts are monitored via the discretized form of condition (6), by evaluating $\boldsymbol{q}^k$ and $\boldsymbol{v}^k$, and building vectors $\boldsymbol{z}_{\mathrm{c}}^{k+1} = (z_{\mathrm{c}}^{(1)\,k+1} \ \cdots \ z_{\mathrm{c}}^{(N_{\mathrm{c}})\,k+1}) \in \mathbb{R}^{N_{\mathrm{c}}}$ and $\boldsymbol{z}_{\mathrm{nc}}^{k+1} = (z_{\mathrm{nc}}^{(1)\,k+1} \ \cdots \ z_{\mathrm{nc}}^{(N_{\mathrm{c}})\,k+1}) \in \mathbb{R}^{N_{\mathrm{c}}}$ accordingly.

3.6. The NLP formulation and its solution in CasADi

The simulation problem described by the discretized conditions in Sect. 3.5 is framed as a *nonlinear optimization program* (NLP). Taking inspiration from [42], the nonlinearity of the complementarity conditions is partially tamed by building the objective function as the squared norm of a vector obtained by stacking the two equalities of the friction conditions, i.e. Eqs. (13) and (15). The problem to be solved is then

$$\begin{aligned} \min_{\substack{\boldsymbol{q}^{k+1},\boldsymbol{v}^{k+1},\\ \boldsymbol{c}_{\mathrm{n}}^{k+1},\boldsymbol{c}_{\mathrm{t}}^{k+1},\\ \boldsymbol{\lambda}^{k+1}}} \quad & \left\| \begin{matrix} (\boldsymbol{c}_{\mathrm{t}}^{k+1})^T \left(\widetilde{\mathbf{T}}(\boldsymbol{q}^k)^T \boldsymbol{v}^{k+1} + \mathbf{E}\, \boldsymbol{\lambda}^{k+1}\right) \\ (\boldsymbol{\lambda}^{k+1})^T \left(\mu\, \boldsymbol{c}_{\mathrm{n}}^{k+1} - \mathbf{E}^T \boldsymbol{c}_{\mathrm{t}}^{k+1}\right) \end{matrix} \right\|_2^2 \\ \text{subject to:} \quad & \mathbf{M}(\boldsymbol{v}^{k+1} - \boldsymbol{v}^k) + h\, \mathbf{K}(\boldsymbol{q}^k, \boldsymbol{v}^k) = \widetilde{\mathbf{G}}(\boldsymbol{q}^k) \boldsymbol{c}^{k+1} + h \left[-\nabla \mathbf{V}(\boldsymbol{q}^k) + \boldsymbol{f}_{\mathrm{ext}}^k\right] \\ & \boldsymbol{q}^{k+1} - \boldsymbol{q}^k - h\, \boldsymbol{v}^{k+1} = 0 \\ & 0 \leq \boldsymbol{c}_{\mathrm{t}}^{k+1} \\ & 0 \leq \boldsymbol{\lambda}^{k+1} \\ & 0 \leq \widetilde{\mathbf{T}}(\boldsymbol{q}^k)^T \boldsymbol{v}^{k+1} + \mathbf{E}\, \boldsymbol{\lambda}^{k+1} \\ & 0 \leq \mu\, \boldsymbol{c}_{\mathrm{n}}^{k+1} - \mathbf{E}^T \boldsymbol{c}_{\mathrm{t}}^{k+1} \\ & 0 \leq \boldsymbol{c}_{\mathrm{n}}^{k+1} \leq H \boldsymbol{z}_{\mathrm{c}}^{k+1} \\ & \mathbf{N}(\boldsymbol{q}^k)^T \left(\boldsymbol{v}^{k+1} + \varepsilon\, \boldsymbol{v}^k\right) \geq -H \boldsymbol{z}_{\mathrm{nc}}^{k+1} \\ & \mathbf{N}(\boldsymbol{q}^k)^T \left(\boldsymbol{v}^{k+1} + \varepsilon\, \boldsymbol{v}^k\right) \leq \quad H \boldsymbol{z}_{\mathrm{nc}}^{k+1} \end{aligned} \tag{20}$$

Using $\boldsymbol{q}^k$ and $\boldsymbol{v}^k$ from the k-th step, the NLP in Eq. (20) is solved to find the optimization variables at the $(k+1)$-th step.

For the numerical solution of the problem we used `CasADi` [43], a general purpose simulation and optimization suite which provides several tools to efficiently formulate and solve large-scale optimization problems. For the program at hand, an Interior Point solver is used, namely IPOPT [44], already interfaced through `CasADi`.

4. Simulation results

Since the formulation in Eqs. (20) will be employed to generate ground truth values (in simulation) related to motion with contacts, it is first tested in some conditions chosen to capture the key aspects of contact

dynamics. The aim is to verify: (i) the correct generation of normal forces integrals, both for impulsive and prolonged contact, (ii) that the effects of friction are coherent with the expectations deriving from the observation of true objects in sliding motion, and (iii) that the dissipation of energy, when contact occurs, has a realistic correlation with the type of contact, i.e. continuous for prolonged contact and discontinuous for impulsive contact.

All simulations are run in a condition of *single point contact*. This is due to issues regarding the use of the restitution constraints from Sect. 3.2, namely the fact that they impose the normal velocity for each contact point after the impact. If more than one point of the object has its normal velocity imposed at the same time, the problem is over-constrained, unless all the velocities are compatible with a rigid-body motion, which is usually not the case. This issue, which is addressed in other works such as [37], is only present in the simulation. When we introduce the identification formulation, the need for the restitution constraints is dropped, and so is the requirement for single point contact.

After introducing the test case scenario, i.e. an elliptical object falling in a 2D environment and its geometry, we run simulations in some selected conditions.

First, the values of normal contact impulses are compared with those computed by hand in the simple case of an ellipse falling from a still condition, so to verify their correctness.

Then, a comparison is made with a formulation that exploits, instead of restitution conditions in Eqs. (4), the direct complementarity between normal contact force integral and normal gap $0 \leq c_{\mathrm{n}} \perp g_{\mathrm{n}}(\boldsymbol{q}) \geq 0$. Such formulation is referred to as *Impulse-Gap Complementarity* (IGC), whereas our formulation will be called *Impulse Restitution Complementarity* (IRC). The use of IGC is very common in robotics when dealing with contacts, and this formulation is also the one the authors in [30] (see also references therein) rely on to generate simulations that are then used to validate their identification program. Interestingly, the comparison between IRC and IGC highlights some critical differences that make IRC a more realistic representation of contact dynamics. Some critical aspects of the IGC have already been discussed in [37], the most crucial being that the values of contact impulses are a random function of the time step h, and that the contact tends to generally mimic a perfectly inelastic behavior. For the above reason, when comparing our result with the IGC, we set $\varepsilon = 0$ in the IRC. The above-mentioned aspects are discussed in Sect. 4.2.

The focus is then moved to the IRC alone. Here, the effects of friction (Sect. 4.3) and energy restitution (Sect. 4.4) are isolated, so to verify whether the respective motion and energy dissipation are realistic.

The simulations are run on an ellipse with semi-axes $a = 1.5$ m and $b = 1$ m, mass $m = 10$ kg and moment of inertia $J = 2\ \mathrm{kg\,m^2}$.

4.1. Test case scenario

Having selected an ellipse as our test object, we can explicitly show the geometric quantities that will be used in the simulation.

With reference to Figure 5, we attach a local frame $\{S_l\} = \{G; x_l, y_l\}$ to the ellipse, centered in its COM G and aligned with its semi-axes a and b. The ellipse's boundary is then described by its local parametric equations

$$\begin{cases} x_{\mathrm{l}}(\beta) &= \rho(\beta) c_\beta \\ y_{\mathrm{l}}(\beta) &= \rho(\beta) s_\beta, \end{cases}$$

where $\rho(\beta)$ is the local ellipse's radius

$$\rho(\beta) = \frac{ab}{\sqrt{b^2 c_\beta^2 + a^2 s_\beta^2}},$$

β is the parametric coordinate and where the shorthand notation $c_{(\cdot)} = \cos(\cdot)$ and $s_{(\cdot)} = \sin(\cdot)$ has been introduced. The coordinates of point G in the global frame $\{S\} = \{O; x, y\}$ and the orientation of the ellipse are stacked in the configuration vector $\boldsymbol{q} = (x \quad y \quad \theta)^T$, introduced in Sect. 3.1.

We model the environment as a single line segment, with a starting point $P_0 = (x_0, y_0)$ and forming an angle α ($\alpha < 0$ in Figure 5) with respect to the horizontal direction x. The signed distance $l(\beta)$ between a

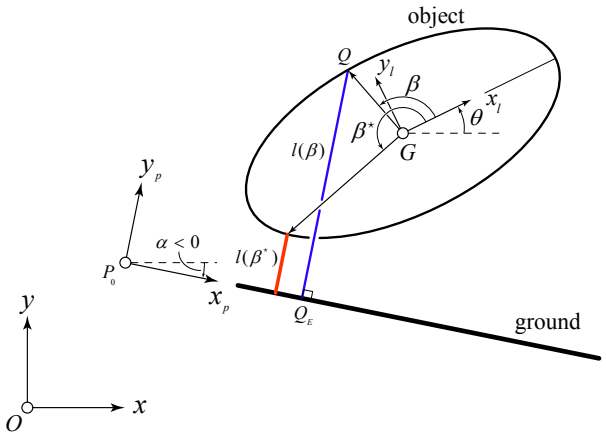

Figure 5: Definition of the normal gap g_n. For a given object configuration $\boldsymbol{q} = (x\ y\ \theta)^T$, once the angle $\beta^\star$ corresponding to the minimum of generic distance $l(\beta)$ is computed, the normal gap g_n can be evaluated as $g_\mathrm{n}(\boldsymbol{q}) = l(\beta^\star)$.

point Q on the ellipse's boundary and its projection Q_E on the environment is computed as the y_p component, with respect to the auxiliary frame $\{S_p\} = \{P_0; x_p, y_p\}$, of vector QQ_E as follows

$$l(\beta) = (y - y_0)c_\alpha - (x - x_0)s_\alpha + \rho(\beta)s_{(\beta+\theta-\alpha)}. \tag{21}$$

Extremizing $l(\beta)$ by computing where $\frac{\partial l(\beta)}{\partial \beta} = 0$, we find the two angles β_1 and β_2 such that

$$\tan\beta_1 = \tan\beta_2 = \left(\frac{b}{a}\right)^2 \frac{1}{\tan(\theta - \alpha)}.$$

The sought for angle $\beta^\star$, which actually minimizes $l(\beta)$, can then be selected as follows

$$\beta^\star = \arg\min\left[l(\beta_1), l(\beta_2)\right].$$

For the given configuration $\boldsymbol{q}$, the normal gap $g_\mathrm{n}(\boldsymbol{q})$ used in our formulation is then calculated as $l(\beta^\star)$. Finally, by finding the position of the contact point Q with respect to the center of mass G

$$GQ = \begin{pmatrix} \rho(\beta^\star)c_{(\theta+\beta^\star)} \\ \rho(\beta^\star)c_{(\theta+\beta^\star)} \end{pmatrix},$$

and properly transforming it in the global frame $\{S\}$, we are in a position to build the needed wrench bases $\mathbf{N}(\boldsymbol{q}) \in \mathbb{R}^{3\times 1}$ and $\widetilde{\mathbf{T}}(\boldsymbol{q}) \in \mathbb{R}^{3\times 2}$, whose expressions are

$$\begin{aligned} \mathbf{N}(\boldsymbol{q}) &= \begin{pmatrix} \boldsymbol{n} \\ \boldsymbol{k}\cdot(GQ \times \boldsymbol{n}) \end{pmatrix} \\ \widetilde{\mathbf{T}}(\boldsymbol{q}) &= \begin{pmatrix} \vec{d}_+ & \vec{d}_- \\ \boldsymbol{k}\cdot\left(GQ \times \vec{d}_+\right) & \boldsymbol{k}\cdot\left(GQ \times \vec{d}_-\right) \end{pmatrix}, \end{aligned}$$

where $\boldsymbol{n}$ is the normal unit vector of the frame attached to contact point Q (see Sect. 3.1), $\vec{d}_+$ and $\vec{d}_-$ are the direction unit vectors of the 2D friction pyramid introduced in Sect. 3.4 and $\boldsymbol{k}$ is a unit vector that is perpendicular to the $x - y$ plane ($\boldsymbol{k} = \vec{d}_+ \times \boldsymbol{n} = -(\vec{d}_- \times \boldsymbol{n})$).

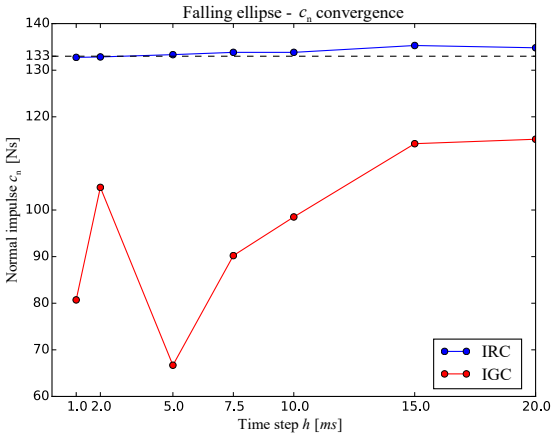

Figure 6: Peak values of the impulse c_n, in function of the time step h used for the discretization, found with the IRC formulation (*blue* line) and with the IGC formulation (*red* line) for the case of ellipse falling from an altitude of 10 m with perfectly inelastic contact (for $h = 1, 2, 5$ ms the shape of c_n is also plotted in Figure 7). The IRC shows convergence when reducing h and a tendency to always give a good approximation of the true c_n, whereas the IGC yields random values of peak c_n, with no apparent convergence for smaller h.

4.2. Normal contact impulse

The first tests are aimed at comparing the values of normal contact impulses generated with the IRC and with the IGC. Firstly, we simulate an ellipse falling from a still condition with orientation $\theta_0 = 0$, with initial height $y_0 = 10$ m.

In this special case, the true value of the contact impulse, used to validate the simulated results, can be easily computed by hand. For a *perfectly inelastic* contact, the contact point of an ellipse with minor semi-axis b impacts the ground with a velocity $\dot{g}_\mathrm{n}^- = -\sqrt{2g\,\Delta y}$, with $\Delta y = y_0 - b$, coming to a complete stop, i.e. $\dot{g}_\mathrm{n}^+ = 0$. The impulse associated with this motion is computable as

$$c_\mathrm{n} = \int_{\dot{g}_\mathrm{n}^-}^{\dot{g}_\mathrm{n}^+} m\,\mathrm{d}v = m\left(\dot{g}_\mathrm{n}^+ - \dot{g}_\mathrm{n}^-\right) = m\sqrt{2g\,(y_0 - b)} \simeq 133 \text{ Ns}, \tag{22}$$

where m is the mass of the ellipse and g is the absolute value of the acceleration of gravity. Considering $c_\mathrm{n} = 133$ Ns as the *true* value, we run simulations for both the IRC and the IGC formulations for different time steps h.

The contact impulse trend, as a function of time step h, is depicted in Figure 6. The value, timing and extension of the contact impulse is shown in Figure 7.

With reference to Figure 7, two main differences are evident: (i) IRC always concentrates the impulse in a single time instant, while IGC distributes the total impulse across two instants (ii) the IRC always yields a good approximation of the true impulse, even for very coarse h, whereas the IGC gives random values for the simulated impulse as h varies.

From the values of the peak impulse computed with different time steps h in Figure 6, it is clear that the impulse computed with the IRC has approximately the same value for every h, converging to the true impulse as $h \to 0$. On the other hand, IGC presents a random peak value for c_n, unrelated to h, which confirms Stewart's statement: *"This does not work: the resulting discretization behaves as if it had a random coefficient of restitution when impacts occur"*, see [37, p.19]).

A second comparison is presented in the case of non zero *initial velocities* of the object, simulating the case of a thrown ellipse, and keeping the contact inelastic ($\varepsilon = 0$ in the IRC). The initial conditions for this example are $\boldsymbol{q}_0 = (0 \quad 5\text{ m} \quad 0)^T$, $\boldsymbol{v}_0 = (10\text{ m/s} \; -3\text{ m/s} \; -8\text{ rad/s})^T$.

The ellipse's resulting motion, which is similar for the IRC and the IGC, is shown in Figure 9. Figure 9(a) presents a time lapse of the complete motion of the ellipse, while Figure 9(b) shows a detail of the first two

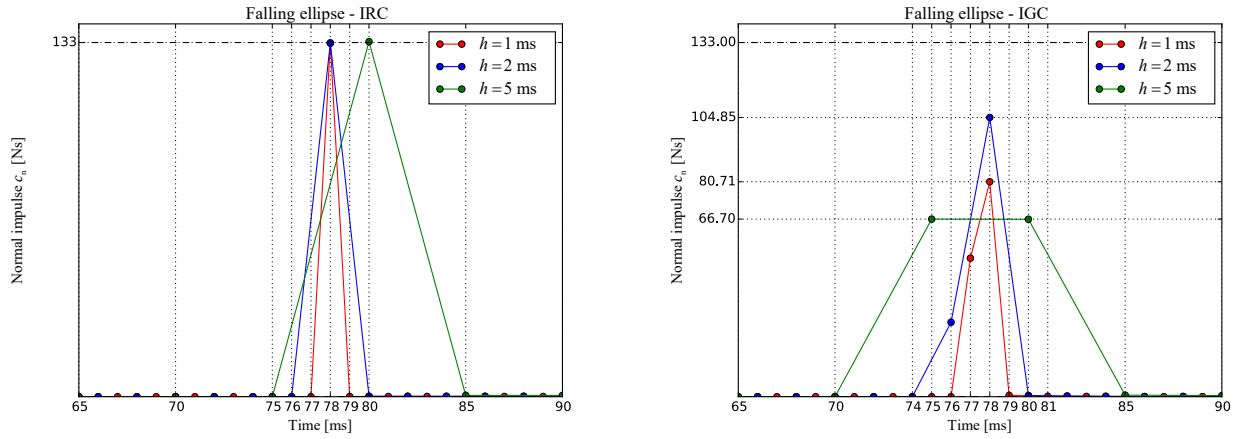

(a) IRC formulation

(b) IGC formulation

Figure 7: Normal impulse c_n generated by the IRC formulation (Figure 7(a)) and by the IGC formulation (Figure 7(b)), for varying time step h, in case of ellipse falling from an altitude of 10 m and subject to perfectly inelastic contact. The *true* value of c_n, computed by hand with Eq. (22), is $|c_n| \simeq 133$ N s. The results show that the IRC formulation always concentrates the impulse in a single time instant ($t = 78$ ms for $h = 1$ ms and for $h = 2$ ms, $t = 80$ ms for $h = 5$ ms), while the IGC splits the total impulse that stops the fall of the object into two time instants. Furthermore, the values of c_n found with the IRC are always a good approximation of the real value, whereas those yielded by IGC are random.

impacts. A video of this simulation is available at [45]. Focusing on the results for the normal impulses relative to the first contact, both for the IRC (Figure 10(a)) and for the IGC (Figure 10(b)), is it possible to come to conclusions similar to Figure 7, as in the case of the ellipse falling horizontally. The IRC concentrates the contact impulse in a single instant, with approximately the same value, even for different h, whereas the IGC yields random values for c_n, again distributed across two time instants, with corresponding impact values that do not show any meaningful trend.

Figure 8 shows that the peak of the impulse for the IRC seems to approach a fixed value ($\simeq 86.5$ Ns), while the IGC shows non-convergent behaviour of the peak c_n as a function of the time discretization h.

4.3. Friction

Due to the poor physical plausibility of the IGC concerning the normal impact representation, we consider it a very unreliable contact model and we omit its analysis for what concerns frictional effects. Therefore, the following analysis are referred only to the IRC model.

The special case of *sliding contact* allows for the isolation of the effects of friction alone.

In this case, we consider an ellipse, already in tangent contact with the environment, with initial conditions $\boldsymbol{q}_0 = (0 \quad 1 \text{ m} \quad 0)^T$, $\boldsymbol{v}_0 = (15 \text{ m/s } 0 \text{ m/s } 0 \text{ rad/s})^T$, such that horizontal component $v_x = 15$ m/s is the only initial velocity. Given the above initial conditions, the first part of the motion is characterized by sliding contact. The simulated ellipse trajectories, for different values of the coefficient of friction in the range $\mu \in [0.3, 0.8]$, are shown in Figure 11. This figure indeed shows a realistic behaviour of the ellipse undergoing frictional contact. Indeed, this does not constitute a proof of the correctness of the model. However, for a general motion like this, since we do not have a ground truth (analytic) trajectory to compare with, only qualitative considerations based on experience are made.

In the first part of the trajectory, the clockwise moment of the frictional force causes a rotational acceleration to the object. For low values of the coefficient of friction, i.e. $\mu < 0.4$, the object starts oscillating while sliding and never loses contact with the ground. On the contrary, for high values of the coefficient of friction, i.e. $\mu \geq 0.4$, enough rotational momentum is gained due to the impulsive nature of the normal force and the object takes a leap. A video of these simulations is available at [45].

Figure 12 shows a plot of the total mechanical energy of the ellipse in the first part of the motion, i.e. in the time range $t \in [0, 1]$ s, for varying μ. It is interesting to observe that the energy dissipation presents a strictly decreasing smooth trend for $\mu \in [0, 0.3)$, as expected for a purely sliding contact with $g_{\mathrm{n}}(\boldsymbol{q}) = 0$. For higher values of the friction coefficient, e.g. in the range $\mu \in [0.4, 1.0]$, the curve presents a steeper slope in the first portion connected with a "kink" to a second constant part representing the ballistic motion of the ellipse ($g_{\mathrm{n}}(\boldsymbol{q}) > 0$), when no energy is dissipated. Of course, when friction is absent ($\mu = 0$), the energy is conserved to its initial value also during sliding.

4.4. Restitution

In this section we highlight how the IRC formulation handles the *energy restitution* after an impact. It is worth stressing that this feature cannot be modelled with formulations adopting direct force-gap complementarity, like the IGC, as discussed in Sect. 4.2.

To this aim, different trajectories of an ellipse thrown with the same initial conditions: $\boldsymbol{q}_0 = (0 \quad 5 \text{ m} \quad 0)^T$, $\boldsymbol{v}_0 = (10 \text{ m/s} \; -3 \text{ m/s} \; -8 \text{ rad/s})^T$ are simulated for different values of the restitution coefficient ε at contact. Figure 13 shows the time lapses of the resulting motions, for $\varepsilon \in [0, 1.0]$. Again, the motion is coherent with experience, as the ellipse bounces progressively higher for increasing ε. A video of these simulations is available at [45].

The trend of the ellipse's total mechanical energy is depicted in Figure 14. The energy dissipation is now discontinuous, as the ellipse instantaneously loses a fraction of energy at each impact encoded by the restitution coefficient ε. Of course, the higher ε the smaller the loss of energy at every impact until, for $\varepsilon = 1$, the impact produces no loss of energy, i.e. a total energy restitution, thus keeping the total mechanical energy constant. It is also worth observing that, due to the instantaneous nature of the impact, the impulsive tangential impact $\boldsymbol{c}_{\mathrm{t}}^k$, resulting from the impulsive normal impact $\boldsymbol{c}_{\mathrm{n}}^k$, has no time interval to dissipate energy through the frictional mechanism: this explains why no other dissipation mechanism is revealed from Figure 14.

5. Identification model

In this section we propose an algorithm that aims to identify the inertial properties of an object undergoing unscheduled contacts with a fixed environment.

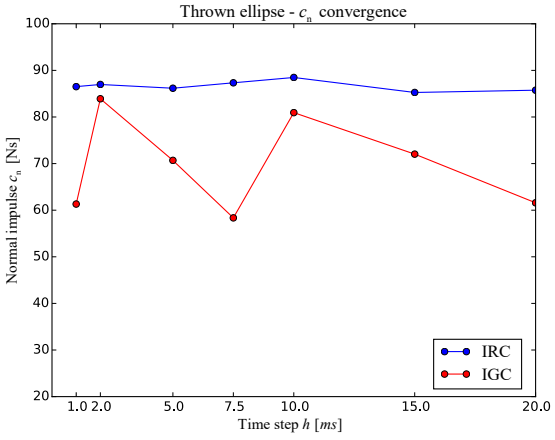

Figure 8: Peak values of the impulse c_{n}, in function of the time step h used for the discretization, found with the IRC formulation (*blue* line) and with the IGC formulation (*red* line) for the case of thrown ellipse with perfectly inelastic contact (for $h = 1, 2, 5$ms the form of c_{n} is also plotted in Figure 10). The IRC shows convergence when reducing h and a tendency to always give approximately the same peak value of c_{n}, whereas the IGC yields random values of peak c_{n}, whit no semblance of convergence for smaller h.

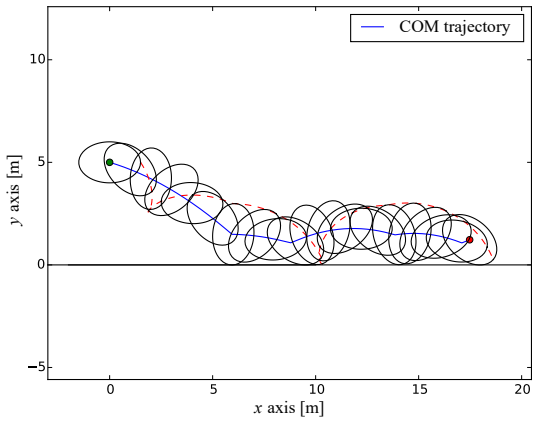

(a) Motion of the thrown ellipse

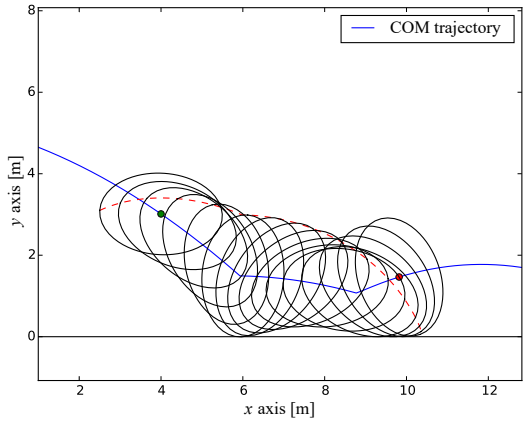

(b) First two impacts of the motion

Figure 9: In Figure 9(a), the motion of a thrown ellipse is shown, simulated with the IRC formulation for the case of perfectly inelastic contact ($\varepsilon = 0$). The IGC yields a similar motion, the differences between the two formulations being mainly in the contact impulses (Figs. 10(a) and 10(b)), and in the impossibility, for the IGC, to vary the restitution of energy at contact (see Sect. 4.4). In Figure 9(b), a detail of the motion, capturing the first two impacts of the ellipse with the ground. The *blue* line follows the trajectory of the ellipse's COM, while the *red dashed* line shows the trajectory of a reference point of the ellipse, so to better visualize the rotation of the object.

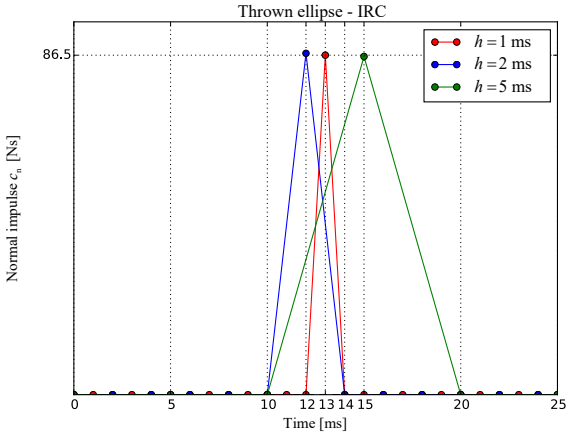

(a) IRC formulation

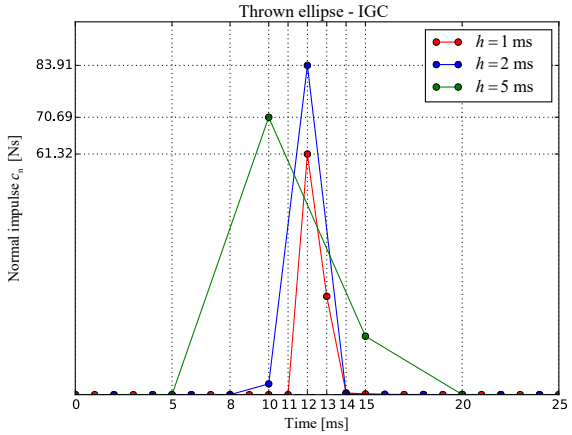

(b) IGC formulation

Figure 10: Normal impulse c_n generated by the IRC formulation (Figure 10(a)) and by the IGC formulation (Figure 10(b)), for varying time step h, in case of ellipse thrown with initial conditions $\boldsymbol{q}_0 = (0 \quad 5\text{ m} \quad 0)^T$, $\boldsymbol{v}_0 = (10\text{ m/s} \; -3\text{ m/s} \; -8\text{ rad/s})^T$ and subject to perfectly inelastic contact. The results show that the IRC formulation always concentrates the impulse into a single time instant ($t = 13$ ms for $h = 1$ ms, $t = 12$ ms for $h = 2$ ms and $t = 15$ ms for $h = 5$ ms), while the IGC splits the total impulse into two time instants. Although a *real* value for the normal impulse has not been computed, the values of c_n found with the IRC are always approximately the same ($|c_n| \simeq 86.5$Ns), supposedly close to the real one. Again, the IGC formulation yields random values of c_n.

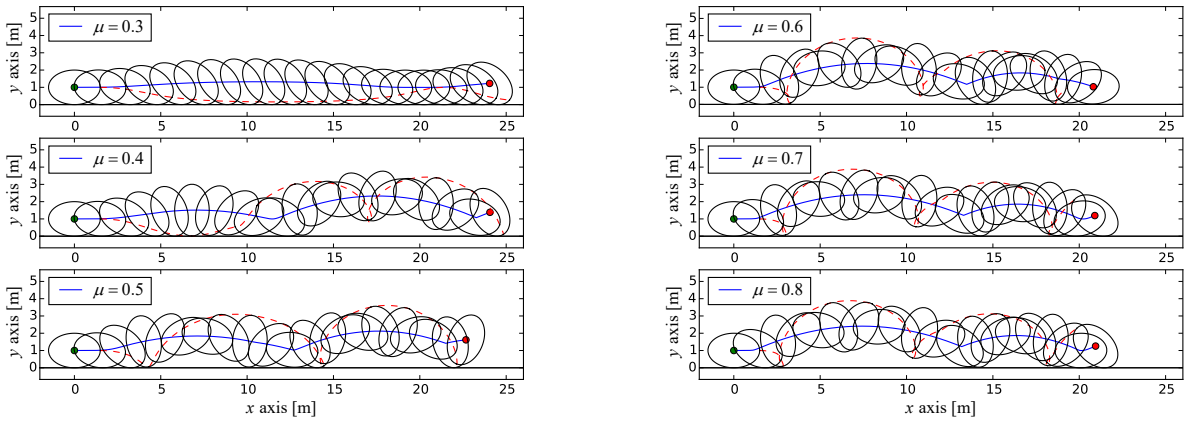

Figure 11: Simulated motion of an ellipse starting with a sliding motion, obtained with the IRC formulation, for different values of the friction coefficient μ. The *blue* line follows the trajectory of the ellipse's COM, while the *red dashed* line shows the trajectory of a reference point of the ellipse, so to better visualize the rotation of the object. Such motion is useful to verify if the effects of friction in the presented simulation are the same to be expected from the sliding motion of a real ellipse. Is is clearly shown that, as in real cases, the friction force has a progressively bigger effect on the motion, as it accelerates the rotation of the object and, for $\mu \geq 0.4$, causes the ellipse to separate from the ground, due to a sufficient gain of rotational momentum.

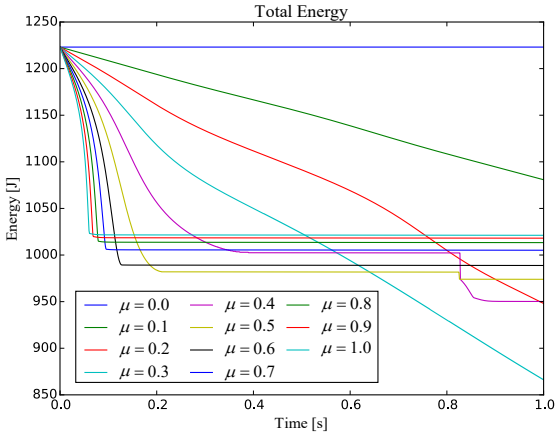

Figure 12: Total mechanical energy of a simulated ellipse starting from a sliding condition. The time lapses of the different trajectories obtained for various values of the coefficient of friction $\mu \in [0.3, 0.8]$ are shown in Figure 11. All simulations are performed with the IRC formulation. This figure shows how friction produces a continuous loss of total mechanical energy, with a steeper curve for higher coefficients of friction μ. The constant portion of the curve represents the ballistic motion of the ellipse. In the case of no friction ($\mu = 0$), the energy is clearly conserved during the whole motion. Such a behaviour concerning energy dissipation is another evidence of the realism of our simulator.

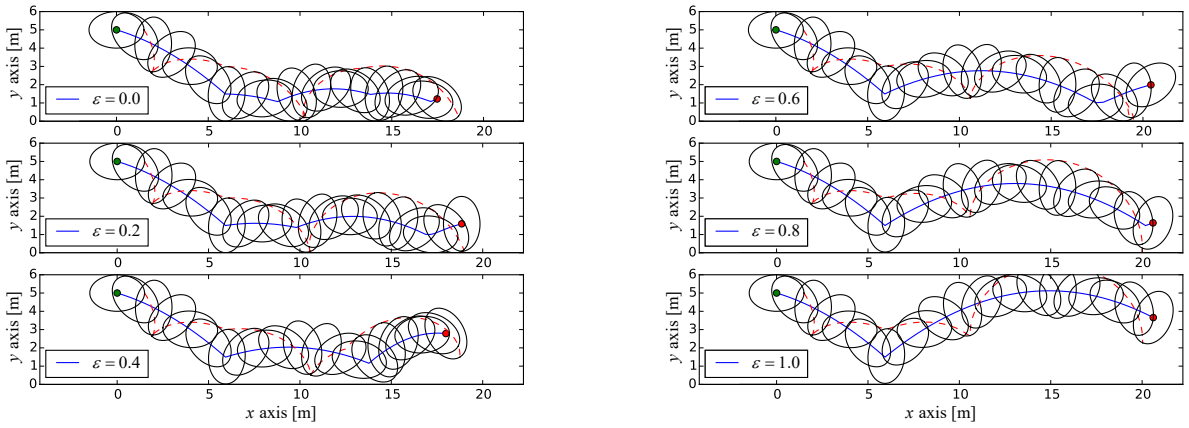

Figure 13: Simulated motion of an ellipse thrown from the height of 5m, with non zero initial velocity ($\boldsymbol{v} \neq 0$), obtained with the IRC formulation, for different values of the restitution coefficient ε. The *blue* line follows the trajectory of the ellipse's COM, while the *red dashed* line traces the trajectory of a reference point of the ellipse, as an aid visualize the rotational motion of the object. Such motion highlights the effects of energy restitution in our simulator, as the impacts on the ground produce higher bounces of the ellipse for increasing values of ε.

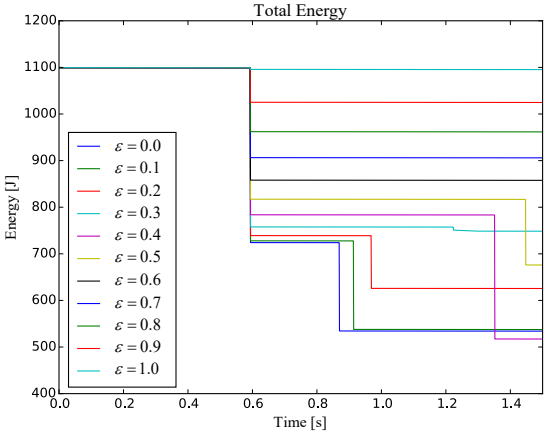

Figure 14: Total energy of different simulations of the same ellipse bouncing on the ground. Each line refers to a different restitution coefficient (for the cases $\varepsilon = 0, 0.2, 0.4, 0.6, 0.8, 1$, the associated trajectories, computed with the IRC formulation, are depicted in Figure 13). The simulations are devised so that no sliding (dynamic friction) occurs, ensuring that the only source of energy dissipation is the restitution coefficient ε. The impulsive contacts generated in this kind of motions produce sudden drops in the energy, which occur in the instant of the impact. The effects of increasing ε are clearly to produce less decrease in the total energy, until, for $\varepsilon = 1$, the energy is conserved throughout the motion, as it is completely restituted to the object at every impact.

More in details, we setup a nonlinear optimization program (NLP) that takes as inputs the measured trajectories of an object and the geometry of both the object and the environment. Then, by properly fitting those trajectories with the simulated trajectory of a virtual object, the program estimates: (i) the sequence of object's states and contact impulses, (ii) its inertial properties, and (iii) the unknown coefficient of friction at the estimated contact points.

It is worth remarking that we improve upon the approach presented in [30], in the following aspects: (i) we do not take the measured postures as ground truth values, as they may be noisy and may violate complementarity conditions. Rather, we find smooth posture estimates that intrinsically verify contact constraints while minimizing the misfit with respect to the measured ones in the least-squares sense. Moreover, (ii) we remove the assumption of perfect knowledge of the friction coefficient and we *concurrently* provide an estimate for it as a by-product of our estimation procedure.

Since the formulation presented in Sect. 3 reproduces the trajectories of an object undergoing impulsive contacts with a good level of realism, all computable quantities obtained from our simulations are used as ground-truth levels in the validation stage of our *identification program*.

5.1. NLP formulation for the identification program

Our identification program builds upon the formulation presented in Sect. 3.5, with the exception that the *restitution conditions* typical of the IRC model in Eqs. (19) are now replaced with the *complementarity conditions*

$$\begin{aligned} \boldsymbol{c}_{\mathrm{n}}^{k+1} &\geq 0 \\ \boldsymbol{g}_{\mathrm{n}}(\boldsymbol{q}^k) &\geq 0 \\ (\boldsymbol{c}_{\mathrm{n}}^{k+1})^T \boldsymbol{g}_{\mathrm{n}}(\boldsymbol{q}^k) &= 0, \end{aligned} \tag{23}$$

typical of the IGC model, where $\boldsymbol{g}_{\mathrm{n}}(\boldsymbol{q}^k) = \begin{pmatrix} g_{\mathrm{n}}^{(1)}(\boldsymbol{q}^k) & \cdots & g_{\mathrm{n}}^{(N_c)}(\boldsymbol{q}^k) \end{pmatrix}^T$ are the normal gap values for pose $\boldsymbol{q}^k$ at time t^k. Since here we are adopting the IGC model, to a distract reader, this choice may appear in contradiction to the need for the IRC model presented and verified in Sec. 4. Actually, no contradiction exists. In fact, while in the simulation process, adopting the IGC model would lead to inexact simulation results, in the estimation process employing the IGC contact model to fit measured object motions is acceptable since the information on the velocity change caused by a normal impulse, and the specific contribution of the restitution coefficient ε, are *already encoded* in the object's observed motion and should not *emerge* from the contact model. On the contrary, avoiding to include the above conditions properly along with Eqs. (19) in the *simulation process*, would ruin physical consistency of both simulated trajectories and impact values, as documented in Sect. 4. Furthermore, as highlighted in [37], the restitution coefficient for real contacts is a function of many factors, such as the orientation of the objects making contact. Assuming a single value of ε for all the contacts would then over-constrain the identification problem, without adding benefits to the physical consistency of the motion.

The current admissible use of the simple complementarity conditions between normal impulse and normal gap suffices in this stage to avoid unphysical interpenetration between the object and the environment.

As anticipated, since the measured trajectories are usually affected by measurement noise, we do not consider them as ground-truth values, but we rather fit them with simulated trajectory by minimizing the squared-norm of a *residual* vector, whose i-th component is defined as follows

$$\boldsymbol{\chi}^i = \boldsymbol{q}^i - \boldsymbol{q}_{\mathrm{m}}^i \in \mathbb{R}^3, \tag{24}$$

where $\boldsymbol{q}_{\mathrm{m}}^i$ is the measured (noisy) trajectory and $\boldsymbol{q}^i$ its smooth estimate at time instant t^i. Depending on the equipment used to capture the motion and its maximum frame rate, we will have only N_{m} measured postures $\boldsymbol{q}_{\mathrm{m}}^0, \ldots, \boldsymbol{q}_{\mathrm{m}}^{N_{\mathrm{m}}-1}$ available in the time window of interest, as shown in Figure 15. However, in order for the simulated trajectory to accurately capture the impact sequence and reproduce a realistic bouncing motion, we use a time discretization h in our program so to have, in the recorded time window, a number N of time instants much larger that the available measurements N_{m}, i.e. $N \gg N_{\mathrm{m}}$.

The selection and pairing of the available estimated postures $\boldsymbol{q}^i$ with the correspondent measurement $\boldsymbol{q}_{\mathrm{m}}^i$ is performed according to the following procedure. Let two subsequent measurements be available after an

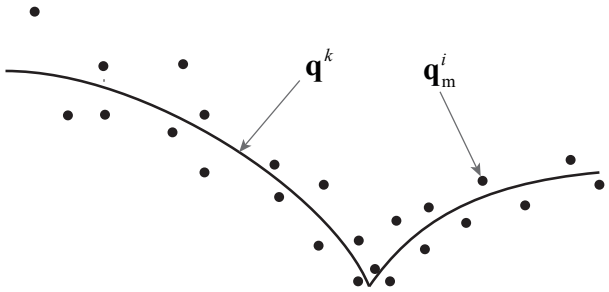

Figure 15: A qualitative example of a best-fit trajectory $\boldsymbol{q}^k$, with $k = 1, \ldots, N-1$, obtained as a result of the identification performed on a series of captured postures $\boldsymbol{q}^i_{\mathrm{m}}$, with $i = 1, \ldots, N_{\mathrm{m}} - 1$.

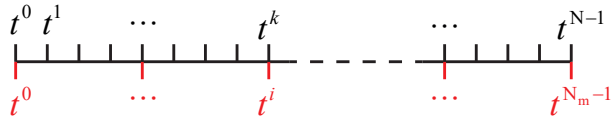

Figure 16: Additional time instants are added between two subsequent captured ones t^i, t^{i+1}, with $i = 1, \ldots, N_{\mathrm{m}} - 1$, in order to reach the desired time step for the discretization used in the identification program.

interval Δt, and let the maximum time step compatible with an accurate simulation be $\bar{h}$. We divide the time interval in a number n_{s} of sub-intervals $n_{\mathrm{s}} = \lceil \Delta t / \bar{h} \rceil$, such that the aligned time step is $h = \Delta t / n_s$, where $h \leq \bar{h}$, thus obtaining a finer discretization. Being t^0 and $t^{N_{\mathrm{m}}-1}$ the time instants corresponding to the first and the last measured postures $\boldsymbol{q}^0_{\mathrm{m}}$ and $\boldsymbol{q}^{N_{\mathrm{m}}-1}_{\mathrm{m}}$, respectively, the identification time window is $T = t^{N_{\mathrm{m}}-1} - t^0$. The actual number of intervals is therefore $N = n_{\mathrm{s}}(N_{\mathrm{m}} - 1)$ and the time step is also given by $h = T/N$.

In order to align the N_{m} measured postures to the $N+1$ simulated postures at time instants t^k, with $k = 0, \ldots, N$, coming from the newly obtained time discretization, Eq. (24) is ultimately written only for a subset N_{m} of the total $N+1$:

$$\boldsymbol{\chi}^i = \boldsymbol{q}^{\frac{N}{N_{\mathrm{m}}-1} \cdot i} - \boldsymbol{q}^i_{\mathrm{m}} = \boldsymbol{q}^{n_s \cdot i} - \boldsymbol{q}^i_{\mathrm{m}} \in \mathbb{R}^3, \tag{25}$$

for $i = 0, \ldots, N_{\mathrm{m}} - 1$. The resulting pairing of time instants is shown in Figure 16.

In order to formulate the NLP we introduce, for each time interval $\left[t^k, t^{k+1}\right]$, a vector comprised by the equalities (complementarities) in Eqs. (18), and Eq. (23):

$$\Gamma^k = \begin{pmatrix} (\boldsymbol{c}^{k+1}_{\mathrm{t}})^T \left(\widetilde{\mathbf{T}}(\boldsymbol{q}^k)^T \boldsymbol{v}^{k+1} + \mathbf{E}\, \boldsymbol{\lambda}^{k+1} \right) \\ (\boldsymbol{\lambda}^{k+1})^T \left(\mu\, \boldsymbol{c}^{k+1}_{\mathrm{n}} - \mathbf{E}^T \boldsymbol{c}^{k+1}_{\mathrm{t}} \right) \\ (\boldsymbol{c}^{k+1}_{\mathrm{n}})^T \boldsymbol{g}_{\mathrm{n}}(\boldsymbol{q}^k) \end{pmatrix} \in \mathbb{R}^3. \tag{26}$$

Then, by employing Eq. (25) and the previously defined Γ^k, we introduce the following two residual vectors

$$\boldsymbol{\chi} = \begin{pmatrix} \boldsymbol{\chi}^0 \\ \vdots \\ \boldsymbol{\chi}^{N_{\mathrm{m}}-1} \end{pmatrix} \in \mathbb{R}^{3N_{\mathrm{m}}}; \quad \Gamma = \begin{pmatrix} \Gamma^0 \\ \vdots \\ \Gamma^{N-1} \end{pmatrix} \in \mathbb{R}^{3N}.$$

By the metric on the residuals defined via the two weighting matrices $\mathbf{W}_{\boldsymbol{\chi}} := \mathtt{diag}(w^1_{\boldsymbol{\chi}}, \ldots, w^{3N_{\mathrm{m}}}_{\boldsymbol{\chi}}) \in \mathbb{R}^{3N_{\mathrm{m}} \times 3N_{\mathrm{m}}}$ and $\mathbf{W}_{\Gamma} := \mathtt{diag}(w^1_{\Gamma}, \ldots, w^{3N}_{\Gamma}) \in \mathbb{R}^{3N \times 3N}$, the NLP for the identification problem takes the form

of the following least-squares minimization:

$$
\begin{aligned}
\min_{\substack{m,J,\mu,\boldsymbol{q}^k,\boldsymbol{v}^k,\\ \boldsymbol{c}_{\mathrm{n}}^{k+1},\boldsymbol{c}_{\mathrm{t}}^{k+1},\boldsymbol{\lambda}^{k+1}}} \quad & \boldsymbol{\chi}^T\mathbf{W}_{\boldsymbol{\chi}}\boldsymbol{\chi} + \Gamma^T\mathbf{W}_{\Gamma}\Gamma \\
\text{subject to:} \quad & \mathbf{M}(\boldsymbol{v}^{k+1}-\boldsymbol{v}^k) + h\,\mathbf{K}(\boldsymbol{q}^k,\boldsymbol{v}^k) = \widetilde{\mathbf{G}}(\boldsymbol{q}^k)\boldsymbol{c}^{k+1} + h\left[-\nabla\mathbf{V}(\boldsymbol{q}^k) + \boldsymbol{f}_{\mathrm{ext}}^k\right] \\
& \boldsymbol{q}^{k+1} - \boldsymbol{q}^k - h\,\boldsymbol{v}^{k+1} = 0 \\
& 0 \le \boldsymbol{c}_{\mathrm{n}}^{k+1} \\
& 0 \le \boldsymbol{g}_{\mathrm{n}}(\boldsymbol{q}^k) \\
& 0 \le \boldsymbol{c}_{\mathrm{t}}^{k+1} \\
& 0 \le \widetilde{\mathbf{T}}(\boldsymbol{q}^k)^T\boldsymbol{v}^{k+1} + \mathbf{E}\,\boldsymbol{\lambda}^{k+1} \\
& 0 \le \boldsymbol{\lambda}^{k+1} \\
& 0 \le \mu\,\boldsymbol{c}_{\mathrm{n}}^{k+1} - \mathbf{E}^T\boldsymbol{c}_{\mathrm{t}}^{k+1} \\
& \text{for } k = 0,\dots,N-1
\end{aligned}
\tag{27}
$$

The NLP in Eq. (27) takes as inputs *only* the measured postures $\boldsymbol{q}_{\mathrm{m}}^i$ in a certain time window, with $i = 0,\dots,N_{\mathrm{m}}-1$, and the geometry of the object-environment system. As a result of the optimization, it yields the best-fit trajectory $\boldsymbol{q}^k$, the contact impulses $\boldsymbol{c}_{\mathrm{n}}^{k+1}$ and $\boldsymbol{c}_{\mathrm{t}}^{k+1}$, with $k = 0,\dots,N-1$, and *concurrently* it estimates the coefficient of friction μ at contact and the object's mass m and moment of inertia J. The problem is solved, again, by using `CasADi` interfaced to the interior point solver IPOPT.

It should be mentioned that, since we do not impose the equality in Eqs. (23) as a hard constraint, but rather add it to the objective function in Eq. (27), its residual will not be exactly zero. The main motivation for this choice is to speed up convergence and handle LICQ deficiency when solving MPECs (mathematical programs with equilibrium constraints) using interior-point methods, as discussed in [46]. As a consequence, the gap does not need to be perfectly closed in order to generate force, and a contact impulse will often be distributed over more than a single time interval. This aspect is highlighted in Sect. 6.1, where simulated impulses are directly compared to the identified ones. However, since our primary objective is to identify the object's inertia, we can accept a slightly rougher estimate of the contact impulses, as long as the reconstructed trajectory is sufficiently close to the captured one. A critical issue is setting matrices $\mathbf{W}_{\Gamma}$ and $\mathbf{W}_{\boldsymbol{\chi}}$ with appropriate values of the weights. Since setting weights is, itself, a fairly open and quite hard problem in general optimization, we chose not to address it in this work. We cannot, therefore, recommend specific strategies; instead, we chose to adopt a general *trial and error* approach, where a set of weights is deemed acceptable when: (i) the time-continuous approximation of the identified posture $\boldsymbol{q}^k$, with $k = 0,\dots,N-1$, is continuous in *all* the observed time window, and differentiable everywhere except where contact occurs — here, there will inevitably be a cusp — (ii) the time-continuous approximation of the identified velocity $\boldsymbol{v}^k$, with $k = 0,\dots,N-1$, is both continuous and differentiable when the object is in free flight, being discontinuous *only* when contact occurs, since its normal component might change direction in the presence of an impulse.

The two afore-mentioned conditions are used as indicators of a physically consistent trajectory connected to a reasonable choice of the weights.

5.2. Identifiability analysis

In this section we sketch an identifiability analysis to motivate the use of a reconstructed trajectory $\boldsymbol{q}$ instead of a measured one $\boldsymbol{q}_{\mathrm{m}}$, the latter being generally affected by measurement noise.

In the first part, we reduce the system's dynamics into a linear form which is easier to analyze. We then search for the set of identifiable parameters. In the third part we discuss the degradation of the identification results due to measurement noise, and motivate the benefical effects of the introduction of a reconstructed trajectory. Lastly, we make observations on the informativeness of a captured trajectory.

5.2.1. Linear form of the dynamics

Since the inertia of a free-flying object is trivially unidentifiable, we limit our analysis to the informative part of the motion, i.e. the time intervals in which contact occurs, and study the case of single contact.

Let the subset of intervals in which contact is active be formed by a number N_I of elements over the total N. The following analysis is also applicable in case of multiple contacts, as long as the considered subset only contains instants with a single active contact. Let us also assume we employ directly the measured trajectory in Eq. (27), under the hypothesis that the number of samples is sufficient. In this manner, the object's postures $\boldsymbol{q}^k$ are known $\forall k$, and velocities $\boldsymbol{v}^k$ are easily computable with $\boldsymbol{q}^{k+1} - \boldsymbol{q}^k - h\,\boldsymbol{v}^{k+1} = 0$. Therefore, $\boldsymbol{g}_\mathrm{n}(\boldsymbol{q}^k)$ and $\boldsymbol{\lambda}^k$ are fixed as well. The only unknown variables are then the object's mass m and moment of inertia J, the contact impulses c_n^k and c_t^k and the coefficient of friction μ.

Under the above hypotheses an analysis of the dynamic equations will be sufficient, since treating c_n^k and c_t^k as unbounded does not affect the qualitative results. For a single time interval $[t^k, t^{k+1}]$, we can write Eq. (16) in the absence of external forces ($\boldsymbol{f}_\mathrm{ext}^k = 0$) as a linear system:

$$\left(\begin{array}{cc|cc} \Delta v_x^k & 0 & -n_x^k & -t_x^k \\ \Delta v_y^k - h\,g & 0 & -n_y^k & -t_y^k \\ 0 & \Delta\omega^k & -\rho_n^k & -\rho_t^k \end{array}\right) \begin{pmatrix} m \\ J \\ c_\mathrm{n}^{k+1} \\ \Delta c_\mathrm{t}^{k+1} \end{pmatrix} = \begin{pmatrix} 0 \\ 0 \\ 0 \end{pmatrix} \tag{28}$$

where $\Delta(\cdot)^k = (\cdot)^{k+1} - (\cdot)^k$, (n_x^k, n_y^k) and (t_x^k, t_y^k) are the components of $\boldsymbol{n}^k$ and $\boldsymbol{t}^k$ in the global frame, $\rho_n^k = \boldsymbol{k} \cdot (GQ^k \times \boldsymbol{n}^k)$ and $\rho_t^k = \boldsymbol{k} \cdot (GQ^k \times \boldsymbol{t}^k)$, $\Delta c_\mathrm{t}^{k+1} = c_{\mathrm{t},+}^{k+1} - c_{\mathrm{t},+}^{k+1}$ is the net value of the tangential contact force and g is the gravitational acceleration, which is the only cause of conservative forces acting on our system — it appears multiplied by the time step h.

If we partition the coefficient matrix in Eq. (28) into two sub-matrices:

$$\mathbf{Y}^k = \begin{pmatrix} \Delta v_x^k & 0 \\ \Delta v_y^k - h\,g & 0 \\ 0 & \Delta\omega^k \end{pmatrix}, \quad -\mathbf{G}^k = \begin{pmatrix} -n_x^k & -t_x^k \\ -n_y^k & -t_y^k \\ -\rho_n^k & -\rho_t^k \end{pmatrix},$$

that is, a sub-matrix $\mathbf{Y}^k$ which is relative to the object's inertia and a sub-matrix $\mathbf{G}^k$ which is the grasp matrix at instant k, we can build the global dynamic matrix for a number N_I of time intervals, as follows

$$\mathbf{A}_{N_\mathrm{I}} = \left(\begin{array}{c|cccc} \mathbf{Y}^1 & -\mathbf{G}^1 & \mathbf{0} & \cdots & \mathbf{0} \\ \mathbf{Y}^2 & \mathbf{0} & -\mathbf{G}^2 & \ddots & \vdots \\ \vdots & \vdots & \ddots & \ddots & \mathbf{0} \\ \mathbf{Y}^{N_\mathrm{I}} & \mathbf{0} & \cdots & \mathbf{0} & -\mathbf{G}^{N_\mathrm{I}} \end{array}\right) \in \mathbb{R}^{3N_\mathrm{I} \times (2+2N_\mathrm{I})} \tag{29}$$

Denoting with $\boldsymbol{w}_{N_\mathrm{I}} = (m \quad J \quad c_\mathrm{n}^1 \quad \Delta c_\mathrm{t}^1 \quad \cdots \quad c_\mathrm{n}^{N_\mathrm{I}} \quad \Delta c_\mathrm{t}^{N_\mathrm{I}})^T \in \mathbb{R}^{2+2N_\mathrm{I}}$ the vector containing the unknown identification variables, the object's dynamics is described by the following homogeneous system of equations

$$\mathbf{A}_{N_\mathrm{I}}\,\boldsymbol{w}_{N_\mathrm{I}} = \mathbf{0} \tag{30}$$

The possibility of estimating vector $\boldsymbol{w}_{N_\mathrm{I}}$ is then reduced to the analysis of matrix $\mathbf{A}_{N_\mathrm{I}}$.

5.2.2. Identifiable set

With the dynamics in the linear form of Eq. (30), we can search for the set of identifiable parameters by observing that, in order for Eq. (30) to have a solution $\bar{\boldsymbol{w}}_{N_\mathrm{I}} \neq \mathbf{0}$, matrix $\mathbf{A}_{N_\mathrm{I}}$ must be rank-deficient.

We start by considering a single time interval, in which the object's dynamics is described by Eq. (28). Matrix $\mathbf{A}^k = (\mathbf{Y}^k | -\mathbf{G}^k) \in \mathbb{R}^{3\times 4}$ has a one-dimensional null space, therefore Eq. (28) has infinite solutions. We can, therefore, only solve for the ratio $\frac{J}{m}$ thus obtaining

$$\frac{J}{m} = \frac{\boldsymbol{k} \cdot \left(GQ^k \times \vec{a}^k\right)}{\Delta\omega^k}, \tag{31}$$

where $\vec{a}^k = \begin{pmatrix} \Delta v_x^k & \Delta v_y^k - h\,g \end{pmatrix}^T$.

Eq. (31), which is simply the *dynamic rotational equilibrium for a rigid body in 2D*, written with respect to the contact point Q^k, has important implications for our analysis. In fact, since m and J are constant properties of the object, Eq. (31) must have the same value for all $k = 0, \ldots, N_\mathrm{I} - 1$, for the motion to be physically consistent. If this is the case, it is possible to choose a reference step, e.g. $k = 0$, and write:

$$\frac{\boldsymbol{k} \cdot \left(GQ^k \times \vec{a}^k\right)}{\Delta\omega^k} = \frac{\boldsymbol{k} \cdot \left(GQ^0 \times \vec{a}^0\right)}{\Delta\omega^0}, \qquad \forall\, k \tag{32}$$

Eq. (32) may be considered as a *physical consistency* condition, that should be verified $\forall k$ whenever $\boldsymbol{q}^k$ and $\boldsymbol{v}^k$ are representative of a real motion.

By applying conditions Eq. (32) to impose physical consistency to the global coefficient matrix $\mathbf{A}_{N_\mathrm{I}}$ $\forall k$, no matter how many time intervals N_I are considered, $\mathbf{A}_{N_\mathrm{I}}$ gains a one-dimensional null space. The homogeneous problem of Eq. (30) has then infinite solutions, in the form $\boldsymbol{w}_{N_\mathrm{I}} = s\,\boldsymbol{\tau}_{N_\mathrm{I}}$, where s is a scalar and $\boldsymbol{\tau}_{N_\mathrm{I}} \in \mathbb{R}^{(2+2N_\mathrm{I})}$ is the base vector of the null space associated with the coefficient matrix $\mathbf{A}_{N_\mathrm{I}}$.

In order to find a scaled solution, one of the components of $\boldsymbol{w}_{N_\mathrm{I}}$ must be imposed, e.g. the object's mass m. In this manner, we can write the sought for solution as

$$\bar{\boldsymbol{w}}_{N_\mathrm{I}} = m\,\bar{\boldsymbol{\tau}}_{N_\mathrm{I}},$$

where $\bar{\boldsymbol{\tau}}_{N_\mathrm{I}} = \begin{pmatrix} 1 & \frac{J}{m} & \frac{c_\mathrm{n}^1}{m} & \frac{\Delta c_\mathrm{t}^1}{m} & \ldots & \frac{c_\mathrm{n}^{N_\mathrm{I}}}{m} & \frac{\Delta c_\mathrm{t}^{N_\mathrm{I}}}{m} \end{pmatrix}^T$.

It is therefore impossible to identify both object's mass m and moment of inertia J separately: in absence of known external forces we need to impose the value of an element of $\boldsymbol{w}_{N_\mathrm{I}}$, i.e. we can only find the ratio between J and m.

5.2.3. Effect of the measurement noise

As a result from Sect. 5.2.2, Eq. (32) is a physical consistency condition that must hold if the trajectory is that of a real object. Since measured trajectories are generally affected by noise, treating them as *true* values in the identification formulation would most likely result in the violation of the physical consistency condition. In particular, if Eq. (32) does not hold, matrix $\mathbf{A}_{N_\mathrm{I}}$ will not be rank-deficient and the only possible solution to Eq. (30) will be $\bar{\boldsymbol{w}}_{N_\mathrm{I}} = \mathbf{0}$, which is clearly a nonsense. This is where the introduction of the error term Eq. (24) proves useful. It gives some measure of freedom to the identification problem, allowing $\boldsymbol{q}^k$ to adapt to the constraints while staying close to the observed motion $\boldsymbol{q}_\mathrm{m}$. As a result, a certain measure of noise is tolerated, i.e. Eq. (32) is satisfied and the represented motion is physically consistent.

5.3. Non-informative trajectories

One last observation can be made on the informative content of the observed trajectories. The analysis presented in the previous sections was made by assuming an informative trajectory, without anomalous drops in the rank of matrix $\mathbf{A}_{N_\mathrm{I}}$ in Eq. (30). There are, of course, trajectories which do not yield enough information to efficiently estimate vector $\boldsymbol{w}_{N_\mathrm{I}}$.

As an example, by looking at the dynamics written for a single time interval (Eq. (28)), we can immediately realize that a motion without angular acceleration ($\Delta\omega^k = 0$), would result in the impossibility of identifying the moment of inertia J, as the second column of the coefficient matrix would become a zero-vector. Analogously, if the linear accelerations are such that the first column of the coefficient matrix becomes a zero-vector, it is impossible to identify the object's mass m.

Since our identification covers a time window with a relatively high number N_I of intervals, the problem is only relevant if the above-mentioned accelerations are absent for the entire observed window, which is a very unlikely situation for a randomly thrown object.

6. Identification results

A double validation of the identification program is performed by using as measured poses of a falling elliptical object both experimental and simulated trajectories, the latter obtained with the IRC formulation illustrated in Sect. 3.6.

Due to the lack of simulated data for multi-point contact, we are still limiting the study to the *single point contact* case. However, it is worth noting that Eq. (27) does not require this limitation. Indeed, as it was pointed out in Sect. 4, the problem with multi-point contact presents itself with the restitution constraints, which are not part of the identification formulation. We find reasonable to expect that, in the case of multiple contacts happening at the same time, the NLP solution will redistribute contact impulses in order to make the identified motion compatible with the captured one. However, since we did not explore this issue deeply, we chose not to embrace this scenario nor to discuss it further.

In the first part of this section, a variety of simulated trajectories for different values of the friction coefficient μ are identified in order to outline a general trend on the capabilities of the identification program. In the second part, our experimental setup for throwing a real elliptical object and recording videos of its trajectories is described. Then, some identification results for experimentally recorded trajectories are presented and discussed.

The elliptical object built for the experiments is laser cut from plywood and has the major and minor semi-axes of length, respectively, $a = 50$ mm and $b = 25$ mm. Its mass is $m = 64$ g, while its moment of inertia with respect to the COM, computed by knowing the geometry and the properties of the material, is $J = 4,84 \cdot 10^4$ g mm^2. The moment of inertia to mass ratio is then $\frac{J}{m} \simeq 756$ mm^2: this value will be considered our ground truth when evaluating the performances of our identification program. The simulated motions will be generated by employing the same object's geometry and inertia.

6.1. Simulated trajectories

In order to mimic a *real* and, therefore *noisy*, capturing process made with a camera, the *ideal* trajectories obtained with the simulation program are modified in two ways: (i) a gaussian noise with a *standard deviation* of 1 mm is added to the simulated trajectory, so to reproduce the effect on the object position and orientation of the error due to the resolution of the camera; (ii) the data from the simulation program are reduced from 240 samples per seconds to 200, 120, 60, 30 samples per second, in order to simulate the effect of having different camera frame rates (*fps* - frames per second).

To outline a trend of the capabilities of the identification program, a generic throw of the ellipse is simulated. In this case the initial conditions are $\boldsymbol{q}_0 = \begin{pmatrix} 0 \text{ m} & 0.1 \text{ m} & -0.785 \text{ rad} \end{pmatrix}^T$, $\boldsymbol{v}_0 = \begin{pmatrix} 3 \text{ m/s} & -5 \text{ m/s} & 0 \text{ rad/s} \end{pmatrix}^T$.

Since ε, μ and *fps* are expected to play a major role in defining the captured trajectory, we find it useful to study how they affect the quality of the identification. From several tests it was quite evident that, given a pre-defined time window, the effect of ε is merely to reduce the number of contact instants, as it increases the object's time of flight. It is then set at $\varepsilon = 0.2$: a value that gives fairly rich trajectories, containing both bounces and sliding motions.

With this value fixed, one test for each combination of μ and *fps* was made, after adding gaussian noise to the simulated trajectories. The resulting identified $\frac{J}{m}$ inertia ratios presented an error with respect to the ground truth which is reported, for each test, in Table 6.1.

The results show that the identification is more accurate (smaller percentage error) for: (i) bigger values of μ: this probably because higher tangential (frictional) impulses cause the motion to be dynamically richer (especially rotation-wise) and thus more informative; (ii) higher *fps*: this because as the number of points to fit with the simulated trajectory increases, the identification program is given less freedom to create outliers in between measured points, as shown in Figure 17.

As an example, the identified contact impulses for the case $\mu = 0.2$, $\varepsilon = 0.2$ and 240 fps along with the ground truth (simulated) values are shown in Figure 18. A video of the identification results in this case is available at [45].

The difference between simulated and identified impulses are due to the issues related to satisfying the equality constraints (in Eqs. (23)) in the least-squares sense by adding them in the objective function of the

μ	30 fps	60 fps	120 fps	200 fps	240 fps
0,1	–72%	–60%	–53%	–48%	–37%
0,2	//	–16%	–5%	+0%	–2%
0,3	–8%	+12%	+4%	+2%	–11%
0,4	–21%	–19%	–4%	–3%	–6%
0,5	–3%	+3%	+1%	–1%	+1%
0,6	+31%	+11%	+0%	+5%	–6%
0,7	+0%	–6%	+5%	+5%	+3%
0,8	+27%	+2%	+8%	+6%	+7%
0,9	+24%	+1%	+1%	+7%	+1%

Table 1: Percentage errors of the identified $\frac{J}{m}$ ratio with respect to the *real* value of 756 mm^2, for varying μ and for different simulated camera *frames per second* (fps).

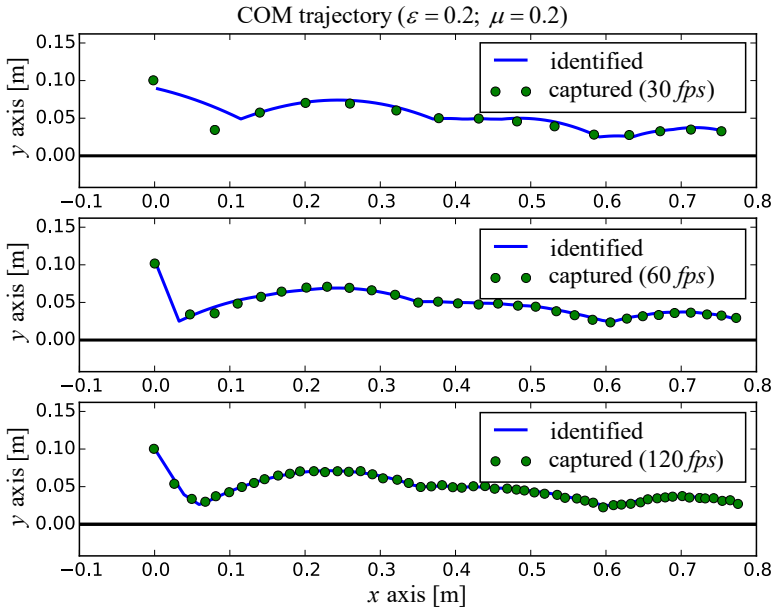

Figure 17: Identified trajectory of the COM, obtained by down-sampling the simulated one to 30, 60, 120 fps and adding artificial noise with a standard deviation of 1 mm, for the case $\varepsilon = 0.2$, $\mu = 0.2$. As the frame-rate increases, the program has more "anchoring" points to comply with and therefore the identified trajectory becomes closer to the real one. Results suggest that a camera with 120 fps is often sufficient for a satisfactory identification of the motion, and Table 6.1 shows how the inertia ratio $\frac{J}{m}$ is correctly identified as well.

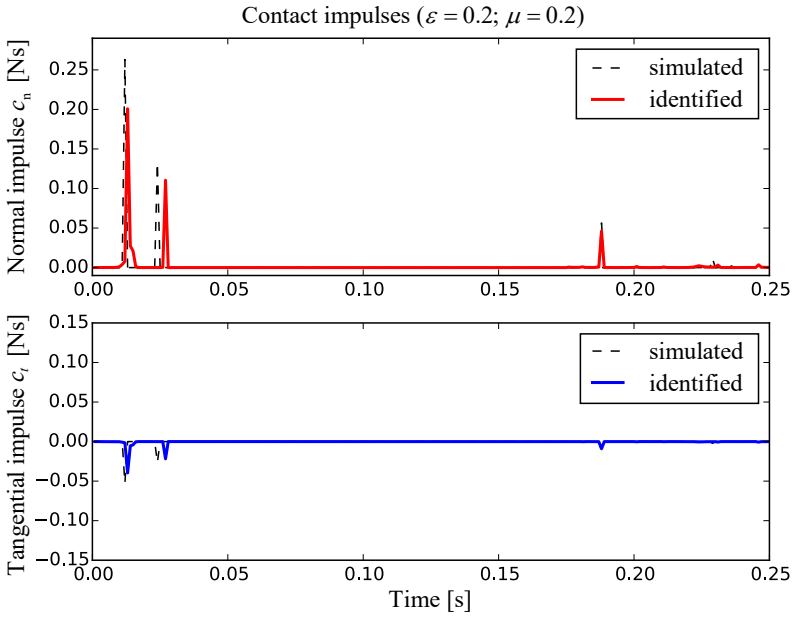

Figure 18: Normal impulse c_n and tangential impulse c_t identified from the simulated motion with $\varepsilon = 0.2$ and $\mu = 0.2$, downsampled at 240 fps and with added artificial noise with a standard deviation of 1 mm. Results are compared with the simulated impulses (black, dashed line).

NLP in Eq. (27), with a penalty approach. Even when the simulated impulse is concentrated in a single time instant, in fact, the identified one is spread over more instants, since the penalty approach does not force the gap to be perfectly zero. The resulting motion, however, is sufficiently close to the simulated one, as shown in Figure 17, and the ratio $\frac{J}{m}$ is estimated correctly.

Since the presented formulation has the peculiar feature of also identifying the coefficient of friction μ, it is worth discussing such aspect as well. Referring to the cases presented in Table 6.1, specifically the ones where inertia is identified within an acceptable confidence level, i.e. for $0.2 \leq \mu \leq 0.9$, the mean values of μ found with the identification formulation follow the trend shown in Figure 19. Such results suggest that beyond a certain threshold, in this case $\mu = 0.6$, the motion of the object becomes of pure rolling, and therefore the absence of sliding hides the effect of the coefficient of friction. When this happens, the identified μ assumes the minimum possible value capable of ensuring pure rolling.

6.2. Real trajectories

In order to test our identification program on a real falling object, we built the experimental setup shown in Figure 20. An elliptical object laser cut from plywood with two holes housing two magnets is constrained to move between two sheets of Polymethyl-Methacrylate (PMMA). This enforces a ballistic 2D motion of the ellipse in the vertical plane, as shown in Figure 20(a). The object can bounce on a wooden bar with adjustable slope, also placed in between the sheets of PMMA.

The ellipse is brought to the desired initial conditions by a simple planar robot (Figure 20(b)), specifically built with low cost components, that ensures the movement of its end-effector in the horizontal and vertical directions. The end-effector, shown in Figure 21, drags the object via two electromagnets, mounted on a rotating head actuated by a servo-motor, and releases it when the desired position is reached, letting it fall on the wooden bar.

The videos of the experiments are shot with a GoPro Hero 4+ camera and then processed with a `MATLAB` algorithm using the Computer Vision System Toolbox. The main functions implemented in the algorithm aim to: (i) correct the fish-eye distortion caused by the standard GoPro lenses, (ii) calibrate the distance

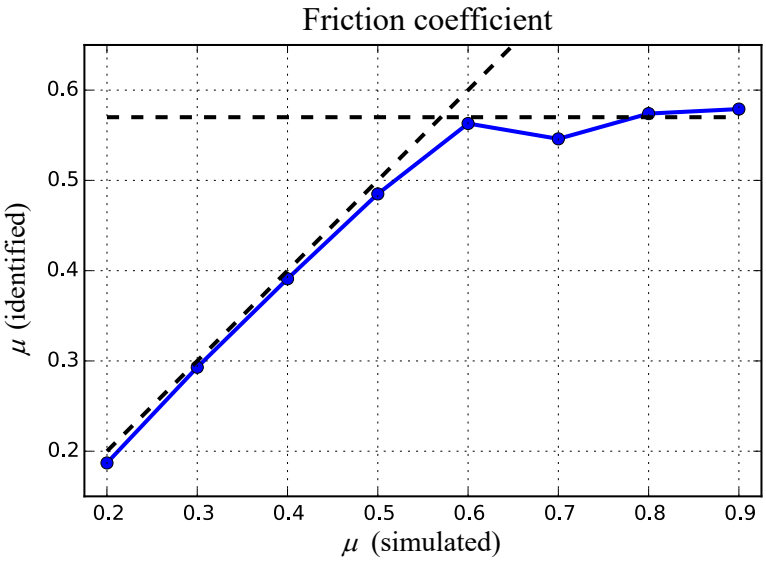

Figure 19: Mean values of the coefficient of friction μ identified from the cases presented in Table 6.1, plotted with respect to the *real* values, used in the simulation program. The identification seems to give good results until, for $\mu \simeq 0.6$, the object no longer slides; from this point on, the identified μ is the minimum possible for the object to ensure rolling without sliding.

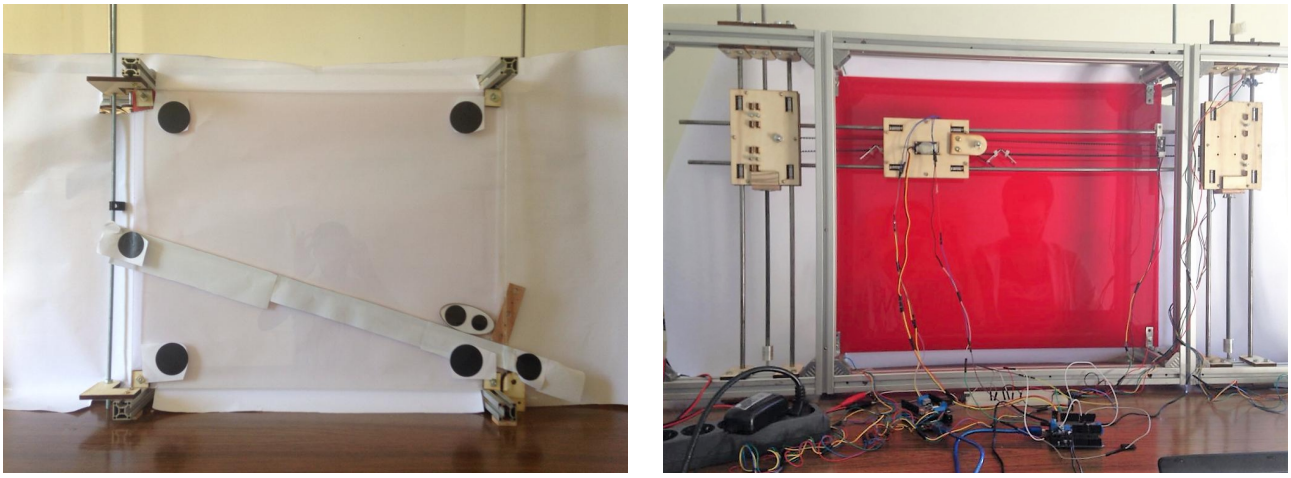

(a) (b)

Figure 20: Experimental set-up used to constrain an ellipse to follow a planar motion. The ellipse falls between two sheets of PMMA, bouncing on a wooden bar with adjustable slope (Figure 20(a)), after being released by a planar robot (Figure 20(b)) which brings it at its initial conditions via the end-effector shown in Figure 21. The motion is captured with a camera and processed with a `MATLAB` algorithm to extract the geometry of the system and the ellipse's posture.

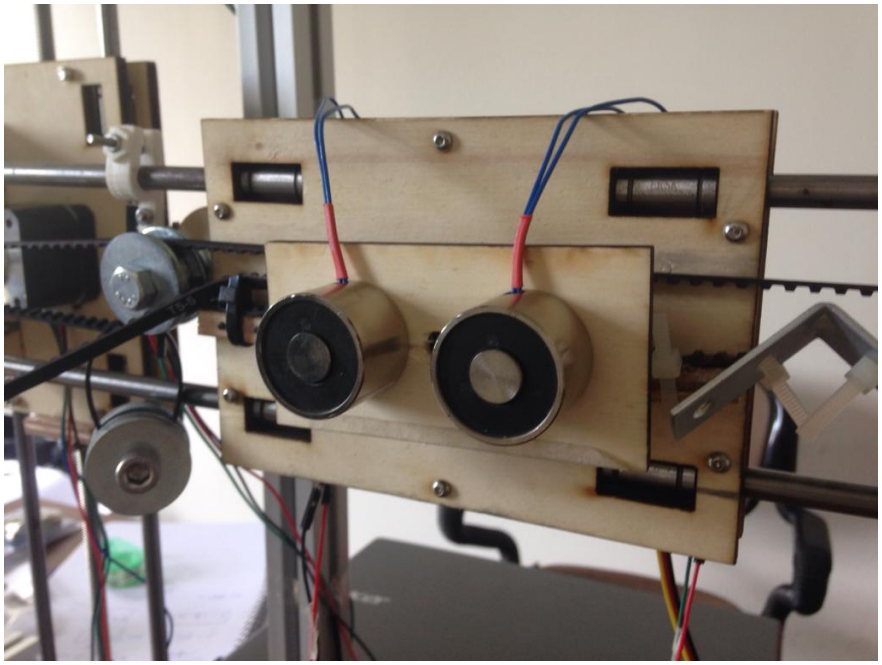

Figure 21: End-effector of the planar robot that drags the ellipse. Two electromagnets (EMs) are fixed on a wooden platform, which is rotated by a servo motor to reach a desired orientation of the object. During the dragging phase the magnetic field of the EMs is set to the same of the ellipse's magnets; when the object must be released, the EMs' field is inverted.

in the experimental setup with respect to video dimensions in pixels, through an appropriate calibration process, and (iii) track the positions of desired entities — in our case simple black circles of the magnets in the ellipse — which are then used to reconstruct the pose of the object.

The back of the structure is covered with white sheets of paper to increase the contrast with the circles and ensure they can be automatically recognized. A total of 8 circles is sufficient: four to define the limits of the workspace and scale the measured quantities, two for the ground segment and two for tracking the pose of the ellipse.

From the computer vision algorithm applied on the video of the experiment, we are able to reconstruct the geometry of the system and the motion of the ellipse, as shown in Figure 22(a). The postures coming from the `MATLAB` algorithm are then passed as input to the identification NLP as a simple `ASCII` file.

As an example, Figure 22(a) shows the time lapse of the identified motion of an ellipse falling for a vertical distance of approximately 20 cm before landing on a bar with a slope of -0.247 rad, with an initial orientation of 0.5 rad. The captured positions of the COM are shown in Figure 22(b), along with the reconstructed trajectory obtained with the identification program in Eq. (27). The identification performed on this motion yields an inertia ratio of $\frac{J}{m} \simeq 778$ mm^2, with an error of 2.9% over the real value ($\simeq 756$ mm^2), while the identified coefficient of friction is $\mu \simeq 0.3$, considered to be a plausible value, as the wood-wood coefficient of friction found in literature is in the range $\mu = 0.25 - 0.5$ (see, e.g. [47]). A video of the identification results on this experiment is available at [45].

The resulting impulses are shown in Figure 23. Although exact values are not available in the real case, it is possible to notice that the identified impulses are comparable to those identified on simulated trajectories (see Sect. 6.1, Figure 18), and that the contact sequence is coherent with the motion shown in Figure 22. The difference lies in the real contacts being "less impulsive", as the wooden bar slightly bends when hit by the object, thus favouring impulses that are smoother then those obtainable with *ideal* rigid-body contacts.

By performing other tests with different initial conditions, the identification program was able to find a mean value of the inertia ratio $\frac{J}{m} \simeq 668$ mm^2, with a *Root Mean Square Error* (RMSE) of 19% throughout all the tests, and a mean value of the coefficient of friction is $\mu \simeq 0.34$, still coherent with the range of values

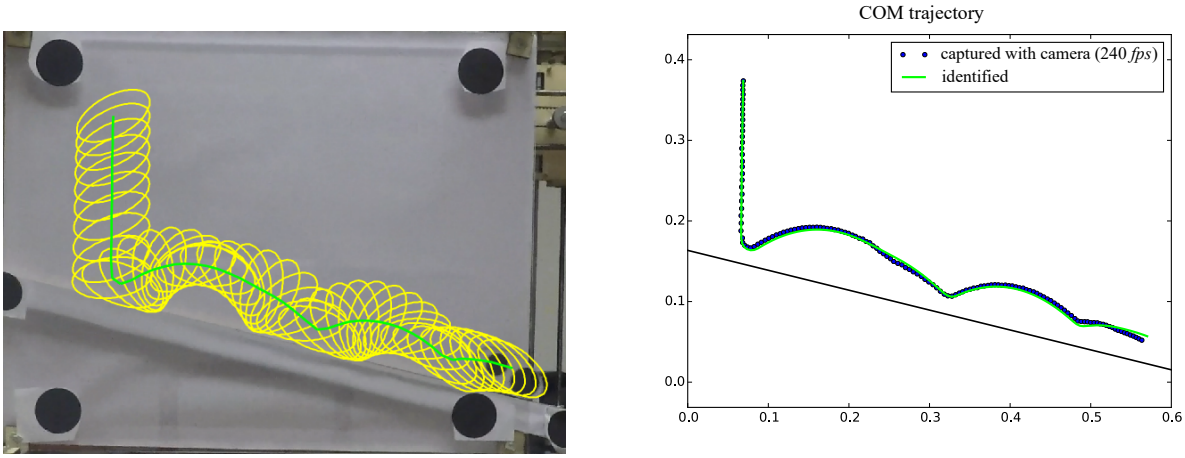

(a) (b)

Figure 22: In Figure 22(a), last frame of the motion of the elliptical object, caught at 240 fps with a GoPro Hero 4+ camera. The time lapse with yellow contours is the *identified* motion obtained with the formulation in Eq. (27); the green line follows the *identified* trajectory of the COM. In Figure 22(b), captured trajectory of the COM at 240 fps, processed via our computer vision algorithm (blue circles) and the resulting identified trajectory (green line).

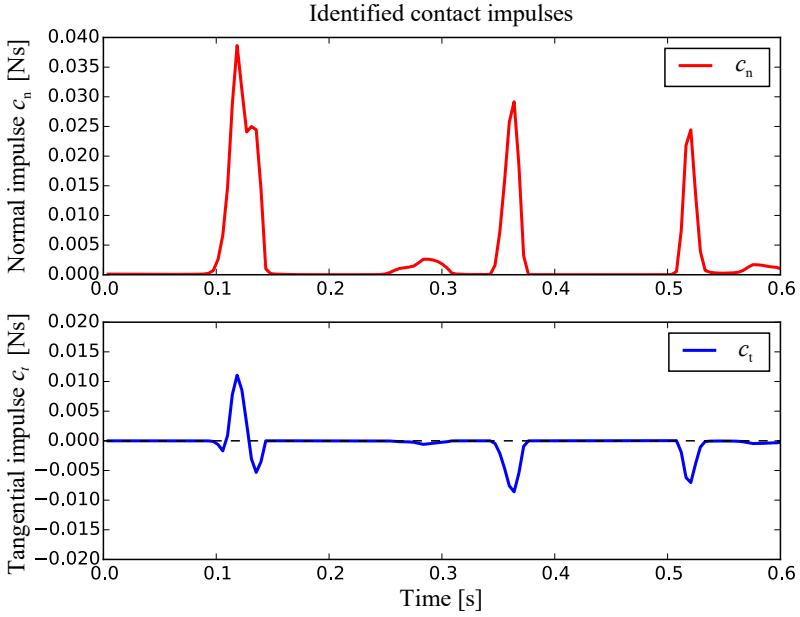

Figure 23: Normal impulse c_n and tangential impulse c_t identified from the real motion shown in Figure 22.

found in literature.

7. Conclusion

This work has addressed the problem of simultaneous state estimation and inertial and frictional parameter identification for planar rigid-bodies subject to *unscheduled* frictional impacts. After presenting the mathematics behind the *simulation* model, a NLP was formulated to solve the problem of simulating the motion of an object undergoing unscheduled contacts in a 2D environment. A thorough evaluation was made on the plausibility of the simulation results. Since our model proved sufficiently realistic, it was used as a generator of ground-truth values for estimating the performances of an *identification* NLP, whose goal was to estimate the states and inertial and frictional parameters of objects captured with a camera. The identification program was tested on a low cost experimental setup, yielding good results both in the state estimation and in the identification of the inertia ratio $\frac{J}{m}$, and the coefficient of friction at contact, even if this latter aspect was not our primary goal.

However, there are a number of open issues that need investigation, as well as improvements to extend the use of our approach. Firstly, a rigorous study on the appropriate weight assignment for the identification NLP in Eq. (27) is recommended, in order to improve the generality of the algorithm. Solving this issue would allow for the possibility of increasing the number of experiments that could be performed in order to validate with more accuracy the identification program.

Then, the case of multiple simultaneous contacts and complex object shapes should be studied, so to broaden the applicability of the presented formulation.

Lastly, an extension to the 3D case would be desirable, although it would require more sophisticated computer vision algorithms for the estimation of the interactions between the object and the environment.

8. Conflicts of interest

The authors declare that they have no conflict of interest.

References

[1] A. Stahl, L. Feigenson, Observing the unexpected enhances infants' learning and exploration, Science 348 (2015) 91–94.

[2] E. A. Wan, R. Van Der Merwe, The unscented Kalman filter for nonlinear estimation, in: IEEE 2000 Adaptive Systems for Signal Processing, Communications, and Control Symposium, IEEE, 2000, pp. 153–158.

[3] Y.-B. J. Y.-B. Jia, M. Erdmann, Observing pose and motion through contact, in: IEEE International Conference on Robotics and Automation, 1998, pp. 723–729.

[4] T. Schmidt, R. Newcombe, D. Fox, DART: dense articulated real-time tracking with consumer depth cameras, Autonomous Robots 39 (3) (2015) 239–258.

[5] T. Schmidt, K. Hertkorn, R. Newcombe, Z. Marton, M. Suppa, D. Fox, Depth-based tracking with physical constraints for robot manipulation, in: IEEE International Conference on Robotics and Automation, 2015, pp. 119–126.

[6] M. C. Koval, N. S. Pollard, S. S. Srinivasa, Pose estimation for planar contact manipulation with manifold particle filters, International Journal of Robotics Research 34 (7) (2015) 922–945.

[7] D. Verscheure, I. Sharf, H. Bruyninckx, J. Swevers, J. De Schutter, Identification of contact parameters from stiff multi-point contact robotic operations, International Journal of Robotics Research 29 (4) (2010) 367–385.

[8] M. Montemerlo, S. Thrun, D. Koller, B. Wegbreit, FastSLAM: A factored solution to the simultaneous localization and mapping problem, in: 18th National Conference on Artificial Intelligence/14th Conference on Innovative Applications of Artificial Intelligence, 2002, pp. 593–598.

[9] L. Zhang, S. Lyu, J. Trinkle, A dynamic Bayesian approach to real-time estimation and filtering in grasp acquisition, in: IEEE International Conference on Robotics and Automation, 2013, pp. 85–92.

[10] S. Kolev, E. Todorov, Physically consistent state estimation and system identification for contacts, in: IEEE-RAS International Conference on Humanoid Robots, Vol. 2015-Decem, IEEE, 2015, pp. 1036–1043.

[11] C. Schedlinski, M. Link, Survey of current inertia parameter identification methods, Mechanical Systems and Signal Processing 15 (1) (2001) 189–211.

[12] R. Almeida, A. Urgueira, N. Maia, Evaluation of the Performance of Three Different Methods Used in the Identification of Rigid Body Properties, Shock and Vibration 15 (3-4) (2008) 467–479.

[13] P. Conti, J. Bretl, Mount Stiffnesses and Inertia Properties from Modal Test Data, Journal of Vibration, Acoustics, Stress, and Reliability in Design 111 (2) (1989) 134–138.

[14] S. M. Pandit, Z. Q. Hu, Determination of rigid body characteristics from time domain modal test data, Journal of Sound and Vibration 177 (1) (1994) 31–41.

[15] P. L. Ringegni, M. D. Actis, A. J. Patanella, An experimental technique for determining mass inertial properties of irregular shape bodies and mechanical assemblies, Measurement 29 (1) (2001) 63–75.

[16] Z. C. Hou, Y. ning Lu, Y. xin Lao, D. Liu, A new trifilar pendulum approach to identify all inertia parameters of a rigid body or assembly, Mechanism and Machine Theory 44 (6) (2009) 1270–1280.

[17] L. Tang, W. B. Shangguan, An improved pendulum method for the determination of the center of gravity and inertia tensor for irregular-shaped bodies, Measurement 44 (10) (2011) 1849–1859.

[18] H. West, E. Papadopoulos, S. Dubowsky, H. Cheah, A method for estimating the mass properties of a manipulator by measuring the reaction moments at its base, in: IEEE International Conference on Robotics and Automation, 1989, pp. 1510–1516.

[19] J. Barreto, L. Muñoz, Inertia parameter identification using a Stewart platform, in: 41st International Symposium on Robotics (ROBOTIK), 2010, pp. 1–8.

[20] M. Niebergall, H. Hahn, Identification of the Ten Inertia Parameters of a Rigid Body, Journal of Nonlinear Dynamics 13 (1997) 361–372.

[21] H. Hahn, M. Niebergall, Development of a measurement robot for identifying all inertia parameters of a rigid body in a single experiment, IEEE Transactions on Control Systems Technology 9 (2) (2001) 416–423.

[22] R. Brancati, R. Russo, S. Savino, Method and equipment for inertia parameter identification, Mechanical Systems and Signal Processing 24 (1) (2010) 29–40.

[23] C. G. Atkeson, C. H. An, J. M. Hollerbach, Estimation of Inertial Parameters of Manipulator Loads and Links, The International Journal of Robotics Research 5 (3) (1986) 101–119.

[24] T. A. Wenzel, K. J. Burnham, M. V. Blundell, R. A. Williams, Dual extended Kalman filter for vehicle state and parameter estimation, Vehicle System Dynamics 44 (2) (2006) 153–171.

[25] S. De Bruyne, H. Van Der Auweraer, P. Diglio, J. Anthonis, Online estimation of vehicle inertial parameters for improving chassis control systems, in: IFAC Proceedings Volumes (IFAC-PapersOnline), Vol. 18, 2011, pp. 1814–1819.

[26] H. S. Bae, J. Ryu, J. C. Gerdes, Road Grade and Vehicle Parameter Estimation for Longitudinal Control Using GPS, Proceedings of the IEEE Conference on Intelligent Transportation Systems (2001) 25–29.

[27] J. Ryu, E. Rossetter, J. Gerdes, Vehicle sideslip and roll parameter estimation using GPS, in: International Symposium on Advanced Vehicle Control (AVEC), 2002, pp. 373–380.

[28] K. Ayusawa, G. Venture, Y. Nakamura, Identification of flying humanoids and humans, in: Proceedings - IEEE International Conference on Robotics and Automation, 2010, pp. 3715–3720.

[29] K. Ayusawa, G. Venture, Y. Nakamura, Identifiability and identification of inertial parameters using the underactuated base-link dynamics for legged multibody systems, International Journal of Robotics Research 33 (3) (2014) 446–468.

[30] N. Fazeli, R. Kolbert, R. Tedrake, A. Rodriguez, Parameter and contact force estimation of planar rigid-bodies undergoing frictional contact, International Journal of Robotics Research 36 (13-14) (2017) 1437–1454.

[31] V. Bonnet, P. Fraisse, A. Crosnier, M. Gautier, A. González, G. Venture, Optimal Exciting Dance for Identifying Inertial Parameters of an Anthropomorphic Structure, IEEE Transactions on Robotics 32 (4) (2016) 823–836.

[32] K. Ayusawa, A. Rioux, E. Yoshida, G. Venture, M. Gautier, Generating persistently exciting trajectory based on condition number optimization, in: Proceedings - IEEE International Conference on Robotics and Automation, 2017, pp. 6518–6524.

[33] J. Moreau, Nonsmooth Mechanics and Applications, Vol. 302 of International Centre for Mechanical Sciences (CISM), CISM Udine, Vienna, 1988, Ch. Unilateral Contact and Dry Friction in Finite Freedom Dynamics, pp. 1–82.

[34] M. Jean, The non-smooth contact dynamics method, Computer Methods in Applied Mechanics and Engineering 177 (1999) 235–257.

[35] E. Drumwright, D. A. Shell, An Evaluation of Methods for Modeling Contact in Multibody Simulation, in: IEEE International Conference on Robotics and Automation, IEEE, 2011, pp. 1695–1701.

[36] R. Featherstone, Rigid Body Dynamics Algorithms, Springer, 2008.

[37] D. E. Stewart, Rigid-Body Dynamics with Friction and Impact, SIAM Review 42 (1) (2000) 3–39.

[38] R. W. Cottle, J.-S. Pang, R. E. Stone, The Linear Complementarity Problem, SIAM, 2009.

[39] A. Richards, J. How, Mixed-integer programming for control, in: American Control Conference, 2005, pp. 2676–2683.

[40] D. E. Stewart, J. C. Trinkle, An implicit time-stepping scheme for rigid body dynamics with inelastic collisions and coulomb friction, International Journal for Numerical Methods in Engineering 39 (15) (1996) 2673–2691.

[41] S. Boyd, L. Vandenberghe, Convex Optimization, Cambridge University Press, 2004.

[42] J. T. Betts, Practical Methods for Optimal Control and Estimation Using Nonlinear Programming, Society for Industrial and Applied Mathematics, 2010.

[43] J. Andersson, A General-Purpose Software Framework for Dynamic Optimization, PhD thesis, Arenberg Doctoral School, KU Leuven, Department of Electrical Engineering (ESAT/SCD) and Optimization in Engineering Center, Kasteelpark Arenberg 10, 3001-Heverlee, Belgium (October 2013).

[44] A. Wächter, L. T. Biegler, On the implementation of an interior-point filter line-search algorithm for large-scale nonlinear programming, Mathematical Programming 106 (1) (2006) 25–57.

[45] M. Gabiccini, F. Fusco, Accompanying video (May 2019).

[46] H. Benson, A. Sen, D. Shanno, R. Vanderbei, Interior-point algorithms, penalty methods and equilibrium problems, Computational Optimization and Applications 34 (June) (2006) 155–182.

[47] D. W. Green, R. H. Perry, Perry's Chemical Engineers' Handbook, McGraw Hill Professional, 2007.